

ARTICLE

Examination of conformational dynamics of AdiC transporter with fluorescence-polarization microscopy

 John H. Lewis¹, Yufeng Zhou¹, and Zhe Lu¹

To understand the mechanism underlying the ability of individual AdiC molecules to transport arginine and agmatine, we used a recently developed high-resolution single-molecule fluorescence-polarization microscopy method to investigate conformation-specific changes in the emission polarization of a bifunctional fluorophore attached to an AdiC molecule. With this capability, we resolved AdiC's four conformations characterized by distinct spatial orientations in the absence or presence of the two substrates, and furthermore, each conformation's two energetic states, totaling 24 states. From the lifetimes of individual states and state-to-state transition probabilities, we determined 60 rate constants characterizing the transitions and 4 K_D values characterizing the interactions of AdiC's two sides with arginine and agmatine, quantitatively defining a 24-state model. This model satisfactorily predicts the observed Michaelis-Menten behaviors of AdiC. With the acquired temporal information and existing structural information, we illustrated how to build an experiment-based integrative 4D model to capture and exhibit the complex spatiotemporal mechanisms underlying facilitated transport of substrates. However, inconsistent with what is expected from the prevailing hypothesis that AdiC is a 1:1 exchanger, all observed conformations transitioned among themselves with or without the presence of substrates. To corroborate this unexpected finding, we performed radioactive flux assays and found that the results are also incompatible with the hypothesis. As a technical advance, we showed that a monofunctional and the standard bifunctional fluorophore labels report comparable spatial orientation information defined in a local frame of reference. Here, the successful determination of the complex conformation-kinetic mechanism of AdiC demonstrates the unprecedented resolving power of the present microscopy method.

Introduction

Transporter molecules adopt four basic types of conformation, namely, externally open (E_o), externally occluded (E_x), internally open (I_o), and internally occluded (I_x) states (Post et al., 1972; Shi, 2013; Krammer and Prévost, 2019). Structural biological studies have revealed structural features underlying these different functional conformations of numerous transporters (Shi, 2013; Krammer and Prévost, 2019). Despite the tremendous progress in functional and structural studies of transporters, some important issues remain. Among them are how to more effectively dissect complex conformational kinetics of transporters, and how to relate the temporal information to the structures of individual states. Addressing these issues requires the capability to track the rapid conformational changes that occur in individual molecules often on an angstrom scale. Furthermore, the temporal measurement at each time point needs to contain the spatial information that specifically identifies the conformational state. Only with relatable kinetic and

structural information, one can fully explain the behaviors of a protein molecule in four dimensions (4D).

Fortunately, as a protein molecule undergoes conformational changes, some of its secondary structures, e.g., α -helices spatially constrained by other secondary structures, inevitably adopt unique spatial orientations in each conformational state. Thus, conformational changes can be tracked by monitoring such an α -helix's spatial orientation defined in a spherical coordinate system by the inclination and rotation angles (θ and ϕ).

To accomplish this task, one can use a polarization microscope to monitor the emission polarization change of a bifunctional rhodamine attached to a suitable α -helix (Sase et al., 1997; Ha et al., 1998; Warshaw et al., 1998; Adachi et al., 2000; Fourkas, 2001; Sosa et al., 2001; Forkey et al., 2003, 2005; Rosenberg et al., 2005; Beausang et al., 2008; Ohmachi et al., 2012; Lippert et al., 2017; Lewis and Lu, 2019a). The documented resolutions of this type of method had been $\geq 25^\circ$ calculated as

¹Department of Physiology, Perelman School of Medicine, University of Pennsylvania, Philadelphia, PA, USA.

Correspondence to Zhe Lu: zhelu@pennmedicine.upenn.edu.

© 2025 Lewis et al. This article is available under a Creative Commons License (Attribution 4.0 International, as described at <https://creativecommons.org/licenses/by/4.0/>).

2.5 times of the standard deviation (σ) of angle distribution (Forkey et al., 2005; Rosenberg et al., 2005; Ohmachi et al., 2012; Lippert et al., 2017). To put this resolution in perspective, the estimated median radius of proteins is \sim 20 Å (Broccieri and Karlin, 2005; Erickson, 2009), and a 1.7 or 3.5 Å change (in the chord distance) would correspond to a rotation of such a radius by only 5° or 10°. Our group increased the effective resolution of θ and φ to 5° and successfully detected the conformational changes in the individual molecules of a K⁺ channel's soluble domain, which occur on angstrom-and-millisecond scales (Lewis and Lu, 2019a, 2019b, 2019c).

Subsequently, we extended this high-resolution polarization microscopy method to studying a membrane protein, namely, the AdiC transporter (Zhou et al., 2023). AdiC naturally facilitates the movement of environmental (L-)arginine (Arg⁺) into enterobacteria and the discharge of agmatine (Agm²⁺) enzymatically generated in a decarboxylation reaction of cytosolic Arg⁺ (Gong et al., 2003; Iyer et al., 2003; Foster, 2004; Fang et al., 2007; Krammer and Prévost, 2019). Elimination of the coproduct CO₂ effectively extrudes proton. Thus, AdiC is a key component of a proton-extrusion system critical for pathogenic enterobacteria to pass a host's gastric barrier, reaching its intestines. Here, we use AdiC to show how to use the microscopy method to investigate highly complex protein conformational kinetics.

Materials and methods

Chemical reagents

Lipids 1-palmitoyl-2-oleoyl-glycero-3-phosphocholine (POPC), 1-palmitoyl-2-oleoyl-sn-glycero-3-phosphoethanolamine (POPE), and 1-palmitoyl-2-oleoyl-sn-glycero-3-phospho-(1'-rac-glycerol) (POPG) were purchased from Avanti Polar Lipids; detergents n-dodecyl- β -D-maltopyranoside (DDM), lauryl maltose neopentyl glycol, sodium cholate, and 3-[(3-Cholamidopropyl)dimethylammonio]-1-propanesulfonate (CHAPS) from Anatrace; monohydrochloride L-[2,3,4-3H]-Arginine and Ultima Gold LLT liquid scintillation cocktail from Revvity; sephadex G-50 resin from Cytiva; bifunctional rhodamine bis-((N-iodoacetyl)-piperazinyl)-sulfonerhodamine from Invitrogen (B10621); and ATTO-550 from ATTO-TEC GmbH; coverslip (#1.5) and microscope slide glass from Thermo Fisher Scientific or VWR; the MSP2N2 cDNA from Addgene (Plasmid #29520) (Grinkova et al., 2010). The AdiC cDNA was synthesized by Integrated DNA Technologies (Zhou et al., 2023). Unless specified otherwise, all other reagents were purchased from Sigma-Aldrich, Thermo Fisher Scientific, or EMD Millipore.

Protein sample preparation, intensity recordings, and data reduction

The following technical aspects have been documented in recent publications (Lewis and Lu, 2019a, 2019b, 2019c; Zhou et al., 2023), which include sample preparation and validation, description of the polarization microscope, the intensity recordings, detection of concurrent changes in the intensities recorded in all four polarization channels using a specific changepoint algorithm, angle calculations, and identification of conformational states using a k-means-clustering algorithm on the basis

of spatial orientations of the attached bifunctional rhodamine probe. The analyses were carried out in LabView with the analytic solutions given in the above references. Following a summary of these methods, we will describe the radioactive flux assay. Additional necessary analysis and calculation methods used in this study, which were performed with the analytical solutions in Mathcad, are described in the supplemental text at the end of the PDF.

The recombinant protein AdiC, which had a biotin moiety linked covalently to the N-terminal biotin ligase recognition sequence and strep tags in both N- and C-terminal regions, the double G188C and S195C cysteine mutations, or a single G188C mutation in helix 6A, and the double C238A and C281A mutation to remove these interfering native cysteines, was produced using the bacterial BL-21 expression system. Purified AdiC, in a buffer containing 50 mM Tris (pH 8), 100 mM NaCl, 2 mM tris(2-carboxyethyl)phosphine, and 2 mM DDM, was mixed with a lipid stock containing 50 mM POPC, 100 mM sodium cholate, 100 mM NaCl, and 20 mM Tris (pH 8), with a molar ratio of 1 AdiC dimer to 1500 POPC molecules. The mixture was rotated at 4°C for at least 1 h. Then, the recombinant MSP2N2 protein in a buffer containing 50 mM Tris (pH 8), 0.5 mM EDTA, 1 mM dithiothreitol (DTT), and 13 mM sodium cholate were added to the mixture to achieve a 1:10 ratio between dimeric AdiC and MSP2N2 (Grinkova et al., 2010). The mixture was further rotated at 4°C for at least an additional hour before detergents were removed from the sample by overnight dialysis at 4°C against an ice-cold buffer containing 100 mM NaCl and 20 mM Tris (pH 8). After dialysis, the AdiC protein in nanodiscs was labeled with biotin and bifunctional rhodamine via the double mutant cysteine residues or monofunctional fluorophore ATTO-550 via the single one. The resulting sample was repurified with size exclusion chromatography as previously described (Zhou et al., 2023).

For fluorescence polarization measurement, the individual labeled AdiC protein molecules, each of which was inserted into a nanodisc, were attached to streptavidin molecules via biotinylated N-termini and strep-tags in both N- and C-terminal regions, streptavidin molecules that had adhered to the surface of a polylysine-coated coverslip. While the sample protein was immersed in a solution (pH 5 unless specified otherwise) containing 100 mM NaCl, 100 mM DTT and 50 mM acetic acid, without or with Arg⁺ or Agm²⁺ at a specific concentration, polarized emissions from individual fluorescent labels, excited in the evanescent field created at the surface of the sample coverslip by a circularly polarized laser beam (532 nm), were collected using a fluorescence microscope (Nikon Ti-E) with a 100 \times oil achromatic objective of a numerical aperture of 1.49, sorted into four polarization emission channels, recorded by an electron-multiplying charge-coupled device (EMCCD) camera (Andor Ixon Ultra 897), and then acquired using the Nikon NIS-Elements software into a Dell PC and stored on its hard drive (Zhou et al., 2023). We summed up the values of individual pixels of a given fluorophore image to obtain the aggregated intensity value, without further analyzing the detailed spatial features of the image itself (Lewis and Lu, 2019a).

I_{tot} , θ , ϕ , and Ω were calculated using Eqs. 11, 12, 13, and 33 in our recent publication (Zhou et al., 2023), respectively. Conformational transitions and states were sequentially identified in two separate steps. A changepoint algorithm (Chen and Gupta, 2001; Beausang et al., 2008) was applied to the intensity traces to detect the transitions between conformational events (Lewis and Lu, 2019a), whereas a shortest-distance-based algorithm (Press et al., 2007) was used to identify the conformational states of individual events on the basis of the information regarding θ and ϕ angles (Lewis and Lu, 2019a). However, operationally, we performed the shortest distance analysis in a Cartesian coordinate system where the x, y, and z values were calculated from the θ and ϕ angles along with a unit radius r (Zhou et al., 2023). To correct for underestimation of θ_L , which stemmed from the wobble motion of the fluorophore dipole, we determined the wobble angle δ through a separate ensemble anisotropy study, as previously described (Lewis and Lu, 2019a). Bifunctional rhodamine-labeled AdiC in nanodiscs was diluted to a final concentration of 40 nM in buffers containing PBS (pH 7.4) and 0–80% glycerol. Fluorescence anisotropy for each sample was measured using a Photon Technology Instruments QuantaMaster fluorometer (Horiba) with 545-nm excitation and 575-nm emission wavelengths. The same protocol was used for ATTO550-labeled AdiC suspended in the detergent lauryl maltose neopentyl glycol (0.1 mM). The resulting δ value was 27.03° for the bifunctional fluorophore and 39.37° for the monofunctional fluorophore.

The fluorescence polarization experiments were performed on 10 separate occasions. Data acquired among these separate collections are statistically comparable and were pooled together, resulting in sufficiently narrow distributions, comparable with those previously illustrated (Zhou et al., 2023). The width of the distributions reflects both technical and biological variations. Outlier data were excluded on the following basis. First, particles whose total intensity exhibited more than one step-bleaching step were excluded. Second, for a given recording, at least 15 events are required to obtain a 95% confidence level for state identification, so any traces with <15 events were excluded on the assumption that the short and long traces belong to the same distribution. Third, for event detection and state identification, a signal-to-noise ratio (SNR) >5 is necessary for the required minimum angle resolution.

Protein reconstitution into lipid vesicles

The lipids POPE and POPG in chloroform were mixed in a 3:1 (wt:wt) ratio, dried using a Buchi Rotavapor R-210 evaporator, stored under vacuum overnight, and resuspended to a final concentration of 20 mg/ml in a pH 7.4 buffer containing 100 mM NaCl, 4 mM N-methyl-D-glucamine (NMG), 1 mM tris(2-carboxyethyl)phosphine, and 10 mM Hepes. The mixture was sonicated in a water bath and mixed with CHAPS to a final concentration of 34 mM. After this mixture was rotated with a tube rotator for >2 h at room temperature, purified AdiC was added to it to achieve an AdiC to lipid ratio of 1:100 (wt:wt). The resulting mixture was rotated for an additional 30 min and then dialyzed three times against a pH 7.4 buffer containing 100 mM NaCl, 4 mM NMG, 1 mM

β -mercaptoethanol, and 10 mM HEPES at room temperature before storing at -80°C.

Arg⁺ uptake assay

Liposomes embedded with AdiC were dialyzed against a buffer containing 20 mM citric acid, titrated to pH 5.0 with KOH, and supplemented with the desired concentration of Arg⁺-HCl and KCl to a combined final concentration of 150 mM. The sample underwent three cycles of freezing and thawing, followed by sonication until becoming homogeneous, and was then passed through Zeba Spin Desalting Columns (2 ml, 40K MWCO; Pierce) equilibrated in the assay buffer containing 100–150 mM NaCl or KCl, 20 mM citric acid titrated to pH 5.0 with NaOH or KOH. This desalting process was repeated as necessary. Immediately after desalting, Arg⁺-HCl was added to achieve the desired concentration while maintaining constant ionic strength, and ³H-Arg⁺ was then added to the sample to a final concentration of 1–3 μ Ci/ml to initiate the uptake reaction (see below for desalting efficiency). At each time point, 50 μ l aliquots of the sample were loaded onto 2.5-ml Sephadex G-50 columns (packed in-house), equilibrated in the assay buffer, and eluted with 1.2 ml of the same buffer into scintillation vials (see below for recovery efficiency of AdiC-containing liposomes). The eluates were mixed with liquid scintillation cocktail and counted using a Beckman LS6500 scintillation counter.

To measure Arg⁺ uptake into liposomes containing no substrate, reconstitution of AdiC into liposomes was performed in 150 mM KCl and 10 mM citric acid, titrated to pH 5.5. Liposomes with AdiC were passed through Zeba Spin Desalting columns equilibrated in 150 mM NaCl and 10 mM citric acid, pH 5.5. Immediately after desalting, a mixture of unlabeled and ³H-labeled Arg⁺ was added to the sample to a final concentration of 2 mM for Arg⁺ and 1 μ Ci/ml for ³H-Arg⁺. Following incubation at room temperature for 2.5 h, 50 μ l aliquots of the sample were processed as described above. Liposomes without AdiC were processed in parallel as negative, background controls.

Efficiency of desalting columns

³H-Arg⁺ was added to the assay buffer to a final concentration of 4 μ Ci/ml. Two 650 μ l aliquots were passed through two Zeba Spin Desalting Columns of 2 ml, equilibrated in the assay buffer. For each sample, a 50 μ l aliquot was taken before and after passage through the columns, mixed with scintillation cocktail, and counted. The ratio of the radioactive counts in the samples before and after desalting gives the desalting efficiency. The desalting columns had an average efficiency of 99.9%. This high efficiency allowed us to accurately set the concentration of Arg⁺ in the bathing solution.

Liposome recovery efficiency of G-50 columns

The experiment was conducted using separate G-50 columns. For each of the three trials, an Arg⁺ uptake assay was carried out as described above. 90 min after the uptake began, each sample of 50 μ l was loaded onto a G-50 column and eluted with 1.2 ml of the assay buffer. In parallel, another 50 μ l sample, as a control, was diluted with 1.2 ml of the assay buffer without going through the G-50 column. Subsequently, 125 μ l of each sample that was eluted from the column or was simply diluted was

passed through a Zeba Spin Desalting Column of 0.5 ml (40K MWCO; Pierce) equilibrated in the assay buffer. Individual samples flowing through from the Zeba columns were mixed with scintillation cocktail and then counted using a scintillation counter. The ratio of the two compared samples yielded an average recovery efficiency of 78% ($\pm 1\%$). This efficiency was used to calculate the actual fraction of radioactive substrate that moved into the vesicles via AdiC.

Volume ratio between the bathing solution and total liposomes

An aliquot of the liposomes prepared for an uptake assay was reserved for determining the volume ratio. The Arg⁺ concentration outside the liposomes was adjusted to match the concentration inside. ³H-Arg⁺ was added to a final concentration of 3 μ Ci/ml. After incubating for 4 h at room temperature, each sample of 50 μ l was loaded onto a G-50 column, eluted, and counted using the same procedure as in the uptake assays. Under such a symmetric concentration condition, the observed maximal fraction of radioactivity, F_{max}^{obs} , moved through AdiC into the liposomes is proportional to the combined volume of the liposomes, whereas the remaining fraction, $1 - F_{max}^{obs}$, is proportional to that of the bathing solution. The ratio of $1 - F_{max}$ and F_{max} gives the outside-to-inside volume ratio, r_v (Eq. 11). In principle, each batch of reconstituted liposomes would have a different volume ratio due to experimental errors. However, we have obtained relatively constant r_v under the same conditions. The mean r_v value was 129 ± 8 for the liposomes containing the wild-type AdiC protein and 110 ± 7 for the liposomes containing the mutant protein.

Statistics

All experimental data were presented as mean \pm SEM. F-tests were used to evaluate single- versus double-exponential fits with the MATLAB-enabled maximum-likelihood estimation tool (Woody et al., 2016). The confidence intervals of simulation data were obtained through the Monte Carlo simulations, and σ is in turn calculated from 68% confidence intervals.

Online supplemental material

Figs. S1, S2, S3, S4, S5, S6, S7, S8, S9, S10, S11, and S12 present additional necessary supporting data. Tables S1, S2, S3, S4, S5, S6, S7, S8, S9, S10, S11, S12, and S13 summarize the equilibrium and kinetic parameters yielded from analyzing the polarization data, or the Michaelis-Menton parameters of the previously observed or model-predicted transport-kinetic behaviors. Videos 1 and 2 exhibit the conformational changes of a single transporter subunit and the 4D model of its conformational dynamics. Supplemental text at the end of the PDF provides the detailed kinetic analysis of data and the derivation of analytic expressions of the conformation-kinetic and transport-kinetic models.

Results

Recordings of fluorescence intensity and determination of fluorophore orientation

We have previously shown the collection and reduction of data from individual AdiC molecules without or with its substrate

Arg⁺ using the polarization microscopy method (Zhou et al., 2023). Because the present kinetic studies require also knowing the behaviors of AdiC bound with Agm²⁺, we will briefly go over the procedures for acquiring data from individual fluorescence-labeled AdiC molecules in the presence of Agm²⁺ and their analysis (Figs. 1, 2, 3, 4, and 5), before illustrating how to extract the kinetic information from the dwell times and state-to-state transition probabilities obtained with or without Arg⁺ or Agm²⁺.

We tracked the orientation changes of a portion of the AdiC molecule through monitoring the emission-polarization changes of a bifunctional rhodamine molecule attached to its helix 6A (Fig. 1 D). This helix adopts differing orientations in different known structural states, such as E₀ and E_x (Fang et al., 2009; Gao et al., 2009, 2010; Kowalczyk et al., 2011; Ilgū et al., 2016, 2021). Helix 6A is attached by the fluorophore via two mutant cysteines, attachments aligning the fluorophore along the helix (Corrie et al., 1998). We chose this labeling site also for it being on the surface of AdiC, minimizing the label's impact on AdiC function so that the acquired information can account for the function. Individual AdiC molecules were inserted into nanodiscs (Ritchie et al., 2009; Grinkova et al., 2010; Denisov et al., 2019), and attached to a coverslip with some flexibility to avoid over restrictions. Thus, the two-fold symmetry axis of individual dimeric AdiC molecules is not expected to align with or to have the same orientation relative to the z_L axis of the usual laboratory (L) frame of reference. Furthermore, the orientation of an AdiC molecule attached to the coverslip was random in the x_L-y_L plane. To solve this problem, we computationally rotated all molecules into a common local frame of reference defined below. All references to AdiC's conformational changes and functions are in the context of a single protomer.

The total intensity (I_{tot}), recorded from an attached rhodamine in the presence of 50 μ M Agm²⁺ during individual 10-ms sampling intervals, was sorted into four polarized components (I_0 , I_{45} , I_{90} , and I_{135} ; Fig. 1 A). Unless specified otherwise, all intensities measurements were obtained at pH 5 for comparison with existing flux-assay data (Tsai et al., 2012). Among their tested pH conditions, a greater fractional uptake occurred with symmetric pH of ~ 5 .

For reference, the relations of φ and θ with the four intensity components, derived for ideal conditions, are given below:

$$\varphi = \frac{1}{2} \tan^{-1} \frac{I_{45} - I_{135}}{I_0 - I_{90}} \quad (1)$$

$$\theta = \sin^{-1} \left[2 \sqrt{\frac{\sqrt{(I_0 - I_{90})^2 + (I_{45} - I_{135})^2}}{(I_0 + I_{90} + I_{45} + I_{135})}} \right] \quad (2)$$

When AdiC transitions between two conformations, the orientation of the attached fluorophore characteristically changes relative to the constant polarization angles of the two polarized beam splitters. For example, should the fluorophore move to increase its φ angle from 0 to 90°, I_0 would decrease, whereas I_{90} would increase, while their sum should remain constant; I_{45} and I_{135} would also change in opposite directions. The concurrent

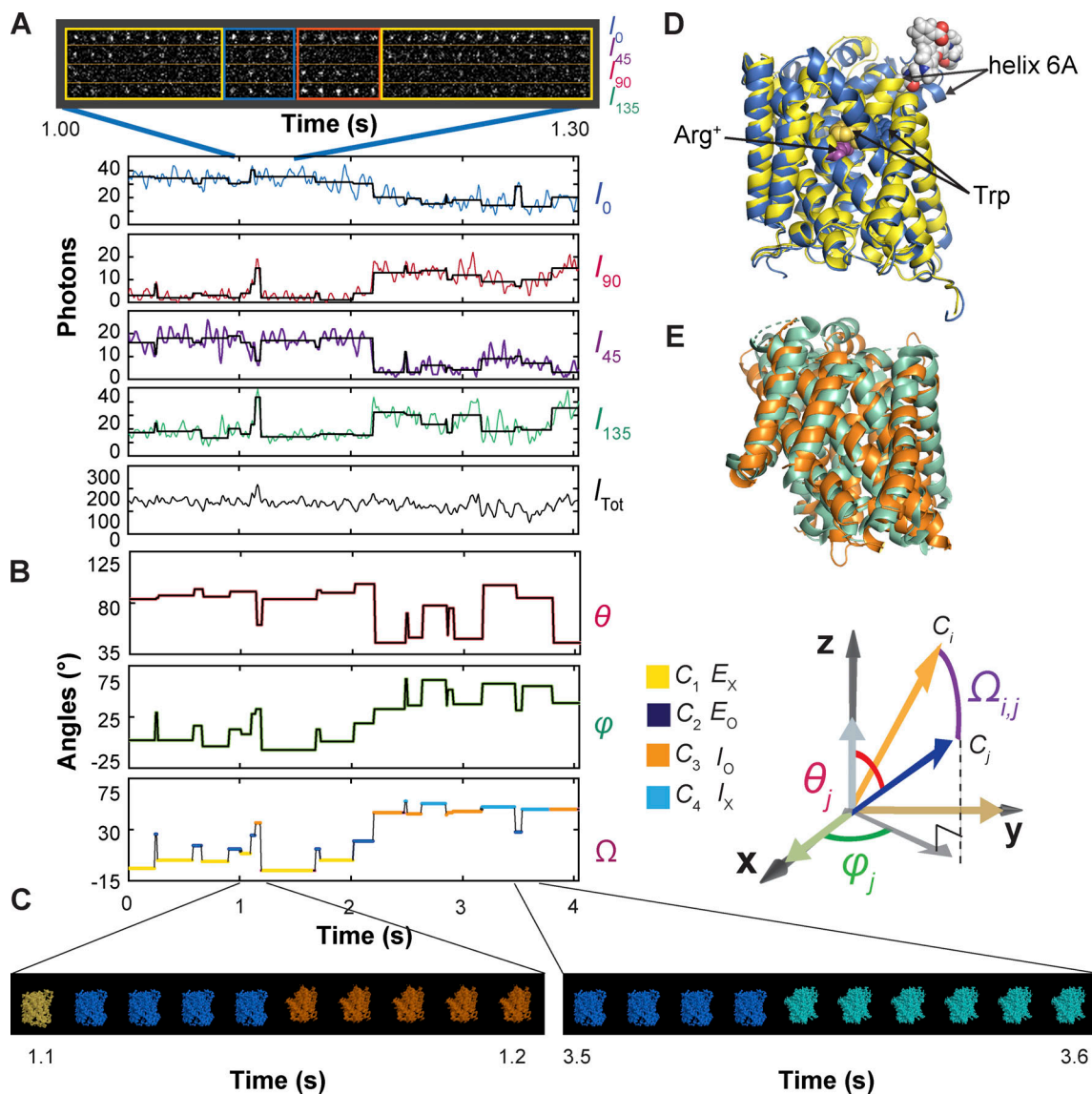


Figure 1. Polarized intensity components of a single fluorescent particle, θ and φ angles calculated from these components, and segments of a video of conformational changes. (A) A segment of consecutive frames of four intensity components (I_0 , I_{45} , I_{90} , and I_{135}) of a bifunctional rhodamine label attached to an AdiC molecule, obtained in the presence of $50 \mu\text{M} \text{Agm}^{2+}$ and pH 5. The integrated values of the recorded intensities color coded for individual components and I_{tot} are plotted underneath against the observation time. Each vertical line in the black traces, superimposed on the colored intensity traces, indicates the time point at which a change in the fluorophore's orientation is identified, whereas each horizontal line represents the mean intensity between two identified consecutive time points. (B) Traces for θ and φ are calculated from the black traces in A and expressed in the local frame of reference defined in Results. Values for the Ω trace are calculated from the θ and φ traces relative to the mean values for C_1 , where the states are color coded. The graphic definition of the angles is shown on the right. (C) Consecutive frames of two segments in Video 1 of AdiC conformational changes in which, as described in Results, the four conformations are represented by the corresponding electron density maps (PDB: 7082, 3L1L, 3GIA, and 6F2G), in accordance with the temporal information encoded in the Ω trace, in which the state identities of individual events are color coded. (D and E) Exhibited in D are spatially aligned structures of E_x and E_0 of AdiC shown with a single subunit (PDBs: 3OB6 and 3L1L), and in E those of I_0 of BasC and I_x of ApcT (PDBs: 6F2G and 3GIA). Helix 6 in E_x of AdiC is attached with a bifunctional rhodamine represented with a space-filling model. The substrate Arg^+ (purple) and a Trp residue (yellow) external to it in E_x of AdiC are represented using space-filling models. The Trp residue (blue) in E_0 points to the opposite direction. Helix 6, Arg^+ , and the Trp residue are all identified by labeled arrows.

changes in four components afford the opportunity for detecting intensity transitions with high confidence.

The vertical black lines superimposed on the recorded intensities indicate the individual time points at which intensity changes occurred (Fig. 1 A). These changes brought about by alterations in the fluorophore's orientation were detected by an algorithm termed “changepoint” (Chen and Gupta, 2001),

adopted here for our case (Lewis and Lu, 2019a). The algorithm tests the two possibilities that a change did or did not occur in the form of their log maximum likelihood ratio with 95% confidence. The program is started by identifying a single transition over the entire trace. If a transition were identified at time point X, it would then search for another single transition between the start of the trace and X or between X and the end. This iterative

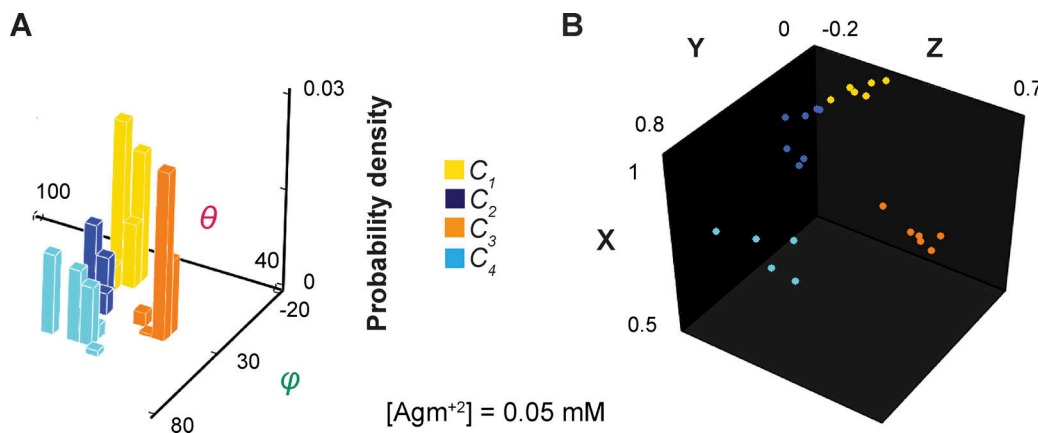


Figure 2. The orientations of the dipole vector of the fluorescence probe in different conformational states in the local frame of reference. (A) The 3D probability densities of individual conformational states plotted against θ and φ values. These angle values for individual events of adopting various conformations are determined from the particle exhibited in Fig. 1. (B) The positions of the arrowheads of individual vectors that represent the orientations of the fluorophore dipole in the individual events are mapped onto a unit sphere defined by the Cartesian coordinates of the local framework described in Results. The x, y, and z positions are calculated from θ and φ plotted in panel A, with a radius of a unit length that has no physical meaning here. The histograms (A) and data points (B) for conformational state C_1 are colored yellow, C_2 colored blue, C_3 colored orange, and C_4 color cyan.

Downloaded from http://jupress.org/jgp/article-pdf/1157/3/e202413709/1939238/jgp_202413709.pdf by guest on 09 February 2026

search process with successively shortened stretches continued until no more transitions were identified. To verify against false positives and refine the positions of individual transition points, we reexamined each identified transition point (e.g., transition t_i) in the region demarcated by t_{i-1} and t_{i+1} (also see below). To check against false negatives, we examined each region demarcated by t_i and t_{i+1} to ensure that no new transitions were identified. For the example shown in Fig. 1 A, the ratio of log maximum likelihood ratio of each identified transition over the 95% confidence threshold expected for the noise level is presented in Fig. S1.

After acquiring this temporal information, averaging the intensities over each dwell time in a particular state markedly increased SNR and thus angle resolution. Each horizontal black line between a pair of consecutive vertical black lines superimposed over the intensity traces corresponds to the mean intensity value during the dwell time (Fig. 1 A). From the traces defined by those black lines, we calculated the angles θ and φ , and then the direct angle change Ω between two states (Fig. 1 B). To calculate θ and φ , we used the expanded versions of Eqs. 1 and 2 (Eqs. 11 and 13 in Zhou et al., 2023) that contain four

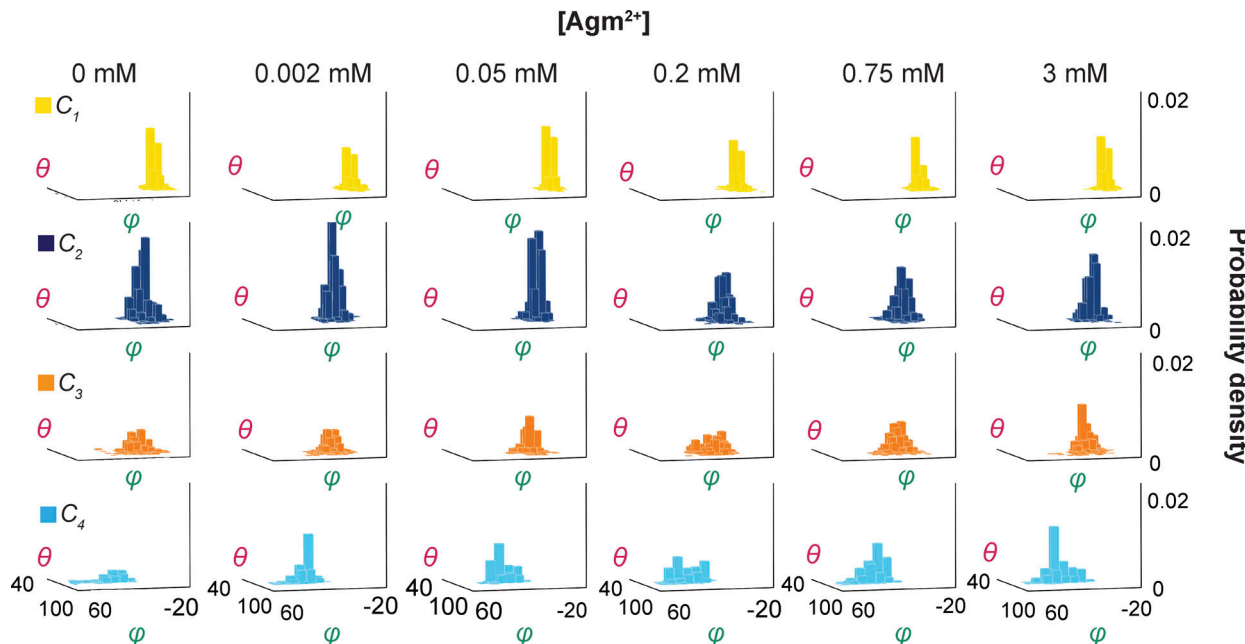


Figure 3. Ensemble 3D probability density distributions of θ and φ in a series of Agm^{2+} concentrations. The θ and φ distributions of four individual states in the absence or presence of the indicated concentrations of Agm^{2+} , in which the value of φ is plotted along the x axis, θ along the y axis, and the probability density along the z axis. Distributions were built with the data analyzed from 34 to 91 particles with a total number (n) of 945–3,187 events. Histogram bars for the conformational state C_1 are colored yellow, C_2 colored blue, C_3 colored orange, and C_4 colored cyan.

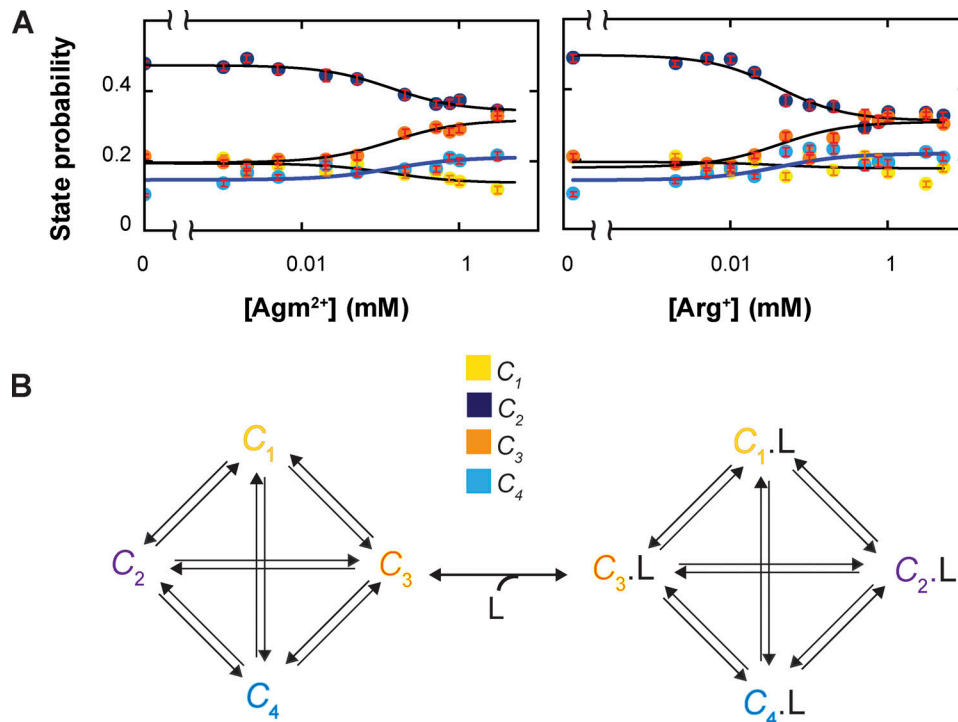


Figure 4. Ligand dependence of the probabilities of conformational states and the diagram of a conformational state model of AdiC. (A) The probabilities of individual four states (mean \pm SEM, $n = 945\text{--}3,187$) are plotted against the Agm^{2+} concentration on a logarithm scale, along with those previously obtained with Arg^+ on the right (Zhou et al., 2023). The curve superimposed on the data for a given conformation represents the predicted relation by the kinetic model (Fig. 6). (B) An eight-state model that accounts for the observed conformational behaviors of AdiC: four apo states and four Arg^+ - or Agm^{2+} -bound states.

predetermined system parameters, including the fast wobble motion of the fluorophore dipole with the half-cone angel δ (Forkey et al., 2005). Because this motion is extremely rapid, a larger δ would be manifested as a lower ratio between the amplitudes of polarized versus non-polarized signals. A lower ratio would in turn be translated to a smaller apparent θ value, which can, however, be corrected with δ determined in an ensemble anisotropy study (see Materials and methods) (Forkey et al., 2000; Lewis and Lu, 2019a).

Given that both angles were calculated here from the ratio of intensities, a change in I_{tot} , due to such a factor as changes in the environment of the fluorophore, would be proportionally reflected in all four polarized components. Consequently, such a change itself would not affect the ratios and thus the determination of the two angles. This approach circumvents the well-known complexity of interpreting the changes in total intensity itself because it depends on the changes in more than one factor, including the aforementioned fluorophore orientation and environment. It is noteworthy that changes in observed I_{tot} contain information regarding changes in θ but not φ , although SNR is too small to deduce the changes in θ in the present case.

Identification of conformational states and analysis of their probabilities

The information encoded in both θ and φ together gives greater resolution of states and confidence in their identification (Fig. 2 A). Operationally, this resolution was performed in a Cartesian

system based on the shortest distance principle, in which x , y , and z coordinates were calculated from θ and φ , with a unity radius r that encodes no meaningful information (Fig. 2 B). The operation was not guided by any preconceived kinetic model with a specific number of states. When two consecutive events were determined to belong to the same state distribution, the transition between them identified by the changepoint algorithm would be considered as a false positive, an example of which is shown in Fig. S1 (orange arrow). These events would then be merged to form a single event.

As previously described for the data collected with or without Arg^+ , the highest number of resolvable states from the data obtained here with Agm^{2+} was also four (Figs. 2 and 3), while maintaining the resolution defined by 2.5σ (Zhou et al., 2023). For communication, we will refer to these states as conformational states $C_1\text{--}C_4$ to distinguish them from structural states, a term reserved for those determined by a structural biology method. As expected, the probability but not the spatial orientation of each state varied with the ligand concentration (Figs. 3 and S2) (Zhou et al., 2023).

The spatial orientations of the fluorophore dipole and thus the tracked helix in C_1 and C_4 were chosen to define the local frame of reference. For all molecules, the local x axis is defined by the orientation in C_1 such that the mean $\varphi_1 = 0^\circ$, and the local x - y plane by those in C_1 and C_4 such that the mean θ_1 or $\theta_4 = 90^\circ$. As such, the local coordinates x , y , and z axes, and thus θ and φ are solely specified by these inherent spatial features of the AdiC

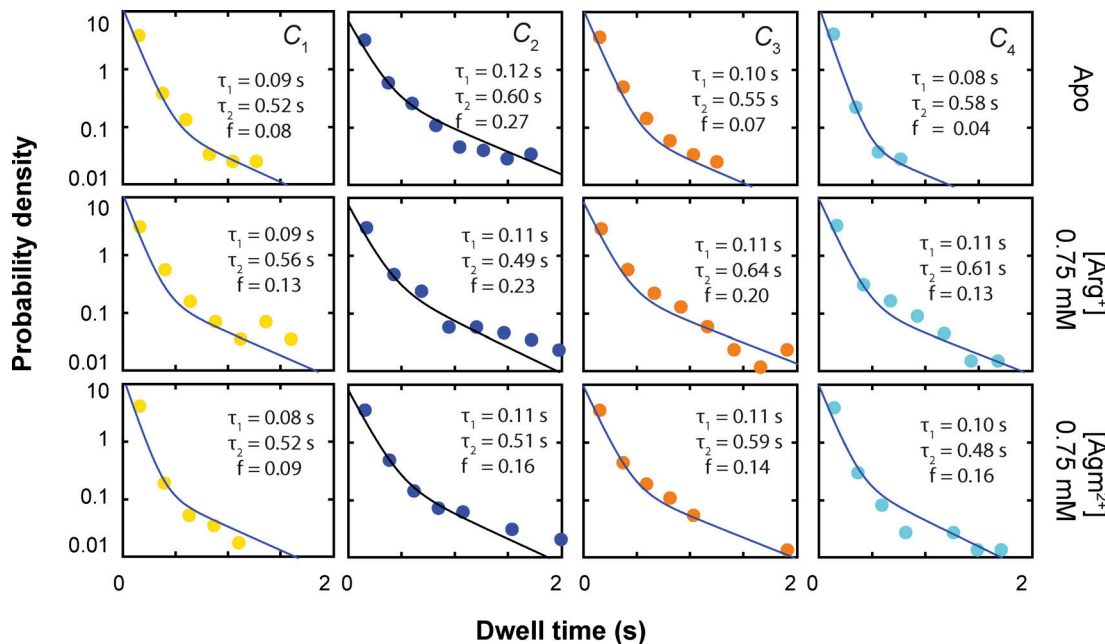


Figure 5. Examples of dwell-time distributions of conformational states. The distributions for C_1 – C_4 in the absence or presence of 0.75 mM Arg^+ or 0.75 mM Agm^{2+} , plotted as the probability density on a log scale against the dwell time of a given state. Each distribution was built from 945 to 3,187 dwelling events. For each state, the fit was performed using a two-exponential equation (Eq. S1) to the data collected over all tested concentrations as a global operation, in which each component is coupled to a ligand-binding model expressed in the same form as Eq. 3.

protein itself. In this local coordinate system common to all examined molecules, we built the θ or φ distribution for individual conformational states of these molecules to determine their statistics and the state probabilities (Fig. 3). All four resolved states exhibited meaningful probabilities without or with Agm^{2+} , characteristics requiring a model of four apo and four ligand-bound states (C_i and ${}^L C_i$) (Figs. 3 and 4). When both Arg^+ and Agm^{2+} are considered, 12 states are required. As with Arg^+ (Zhou et al., 2023), the probabilities of C_2 and C_3 clearly vary with the Agm^{2+} concentration, which should thus be open states) (Fig. 4 A). In contrast, the probabilities of C_1 and C_4 displayed relatively small variations, which may thus not be directly accessible to ligands and be consistent with occluded states. Regarding sidedness, judging from available AdiC's structures alone, the orientations of C_1 and C_2 are consistent with those of E_x and E_o (Table 1). Based on these two sets of information, the relations of C_1 – C_4 to the structural-functional states are consistent with the following assignment: C_1 corresponds to E_x , C_2 to E_o , C_3 to I_o , and C_4 to I_x , a relation observed also in our previous study of AdiC with Arg^+ (Zhou et al., 2023).

We note the following finding revealed originally in that study (Zhou et al., 2023) and observed again here (Fig. S3). The above corresponding relations also turn out in the best fit between the mean orientations of the tracked helix in the four conformational states and those of the crystal structures of AdiC in E_o and E_x , the BasC transporter in I_o , and the ApcT transporter in I_x (Fig. 1, D and E) (Shaffer et al., 2009; Gao et al., 2010; Errasti-Murugarren et al., 2019; Ilgū et al., 2021). These latter two transporters share the same structural fold with AdiC. Among the two sets of four states, there are 24 possible combinations. The best fit combination was determined according to

the largest inverse value of combined least squares (LS_e) among the 24 cases (Fig. S3 C; right arrow). We will evaluate the transport properties of AdiC predicted by the model in this configuration and compare them with those of the configuration with the opposite membrane sidedness, i.e., C_2 corresponds to I_o and C_3 corresponds to E_o (Fig. S3 C; left arrow).

Based on the above information, we generated the temporal template for Video 1, with which we show how to exhibit the conformational changes of a single subunit by matching the states identified here at each time point to their corresponding structural states. Because the structures of AdiC in only E_o and E_x are currently available, the structures of the BasC and ApcT transporters in I_o and I_x states are used as temporary proxies for those of AdiC (Shaffer et al., 2009; Gao et al., 2010; Errasti-Murugarren et al., 2019; Ilgū et al., 2021). Specifically, the temporal template was obtained from the Ω trace in which the states had been identified (Fig. 1 B). The structural states are shown in the form of electron density maps (PDBs: 7O82, 3LL1, 3GIA, and 6F2G) (Shaffer et al., 2009; Gao et al., 2010; Errasti-Murugarren et al., 2019; Ilgū et al., 2021), color coded for states as in the Ω trace. Two segments of video frames from the video are shown in Fig. 1 C. Thus, the video was directly generated from the experimental data without kinetic and structural modeling, showing the spatiotemporal behaviors of a single subunit. Note that due to the limit of allowable file size, the video was made for viewing in a small window.

Construction and analysis of dwell-time distributions of conformational states

Detection of transition points and identification of conformational states enabled us to measure the dwell times of an AdiC

Table 1. Orientations and relative angle changes of the four conformational states of AdiC

	$\theta_1 E_x$	$\theta_2 E_o$	$\theta_3 I_o$	$\theta_4 I_x$
Crystallography ^a	93.8°	83.6°	71.7°	95.3°
Polarization (BF ^b , Agm ²⁺)	90° ± 5.3°	88.7° ± 6.7°	77.4° ± 9.3°	90° ± 5.3°
Polarization (BF ^b , Arg ⁺)	90° ± 4.7°	87.8° ± 7.2°	76.6° ± 9.0°	90° ± 4.5°
Polarization (MF ^c , Arg ⁺)	90° ± 4.6°	89.0° ± 5.5°	79.9° ± 7.3°	90° ± 4.1°
	$\varphi_1 E_x$	$\varphi_2 E_o$	$\varphi_3 I_o$	$\varphi_4 I_x$
Crystallography ^a	-1.89°	20.9°	27.5°	38.7°
Polarization (BF ^b , Agm ²⁺)	0° ± 4.5°	17.9° ± 6.3°	27.2° ± 9.3°	40.5° ± 10°
Polarization (BF ^b , Arg ⁺)	0° ± 4.0°	16.6° ± 7.2°	26.6° ± 10°	38.5° ± 11°
Polarization (MF ^c , Arg ⁺)	0° ± 3.9°	13.7° ± 4.8°	22.7° ± 6.7°	39.5° ± 7.5°

^aIn the structural analysis, the AdiC structures in the states E_o (PDB: 7O82) and E_x (PDB: 3L1L) and the BasC and ApcT structures in the states I_o (PDB: 6F2G) and I_x (PDB: 3GIA) were used. Data are shown as mean ± σ .

^b"BF" indicates the fluorophore rhodamine bifunctionally attached.

^c"MF" indicates the fluorophore ATTO-550 monofunctionally attached.

molecule in individual conformational states. **Fig. 5** exhibits the dwell-time distributions with or without a saturating concentration of Arg⁺ or Agm²⁺. To analyze the distributions, we used an exponential function derived for data recorded with a camera at a constant frame rate (Lewis et al., 2017) (Eq. S1), which also addresses the problem arising from missing short events. Unlike those of MthK's regulatory module (Lewis and Lu, 2019c), the dwell-time distributions of AdiC's four states under all examined conditions are statistically much better fitted with a double-exponential function than a single-exponential function (Eq. S1 versus Eq. S2), based on all P values being $<10^{-15}$ in F-tests (Woody et al., 2016). The distributions could not be fitted with a triple-exponential function without arbitrarily constraining the fitting parameters of some components. In the final analysis of each state, a global double-exponential fit to the entire collection of distributions of dwell times obtained in the presence of all tested concentrations of Arg⁺ and Agm²⁺. As a requirement to achieve the joint fit, the fast and slow components are each coupled to a binding isotherm that informs the concentration dependence of relative amplitude of a given component. Certainly, the fits to data looked better when each distribution was separately fitted because in such an operation, the statistical noise among different experiments to obtain information under different substrate conditions were not taken into consideration.

Given that each of the four conformational states has two identifiable, energetically distinct states, 8 states are required to account for the behaviors of AdiC in the absence or the presence of either ligand type, totaling 24 states (Fig. 6). To reflect this expansion, each of the four conformations in **Fig. 4 B** needs to be split into two energetic states. The two energetic states of C_1 are denoted as S_1 and S_5 , C_2 as S_2 and S_6 , C_3 as S_3 and S_7 , and C_4 as S_4 and S_8 .

The state transition information (Fig. 1), which is necessary for identifying state connectivity, was observed at the level of conformation states, not their underlying energetic states. Thus, the only constrainable model is the one in which one of the two interconnected energetic states of a given conformation directly

communicates with one of the two interconnected energetic states of another conformation, dubbed a serial connection (Fig. 6). When the connectivity among states is considered, there are no other constrainable alternative 24-state models. The building of a serial relation for S_2 and S_6 or S_3 and S_7 , in terms of accessing a third state or the solution, is consistent with the following mechanistic expectation. A ligand-binding process involves at least two steps: an initial second-order reaction step to form a so-called collision complex between the ligand and its receptor, which is typically a near diffusion-limited process, and a subsequent first-order transition to a more stable bound state. In a serial arrangement, S_5 or S_8 does not directly transition to any open states and is effectively an occluded "cul-de-sac" state (see below). Here, the pair of S_1 and S_5 could be reduced back to C_1 , and S_4 and S_8 to C_4 but are separately expressed to reflect the kinetic evidence of their existence.

Determination of rate constants in the framework of the 24-state model

The analysis of the dwell-time distribution of each confirmation for a given ligand condition yields three parameters: the time constants of the first (fast) and the second (slow) components ($\tau_1 = 1/\lambda_1$ and $\tau_2 = 1/\lambda_2$) and the fraction (f) of the amplitude of the first exponential component relative to the total. From these parameters and the state-to-state transition probabilities ($p_{i,j}$) obtained under the corresponding condition, we could extract the underlying rate constants among all relevant states (see supplemental text at the end of the PDF). In such a way, we performed the analysis on data collected in the presence of 13 Arg⁺ concentrations or 11 Agm²⁺ concentrations, including the ligand-free condition. The values of τ_1 , τ_2 , and f obtained for all examined ligand conditions are plotted in **Fig. 7**, and those of $p_{i,j}$ in **Fig. 8**. From these parameters of each conformation, we calculated the 20 apparent rate constants $^{app}k_{i,j}$ for a given ligand condition and plotted them against the Arg⁺ or Agm²⁺ concentration (Fig. 9). Fitting the equation

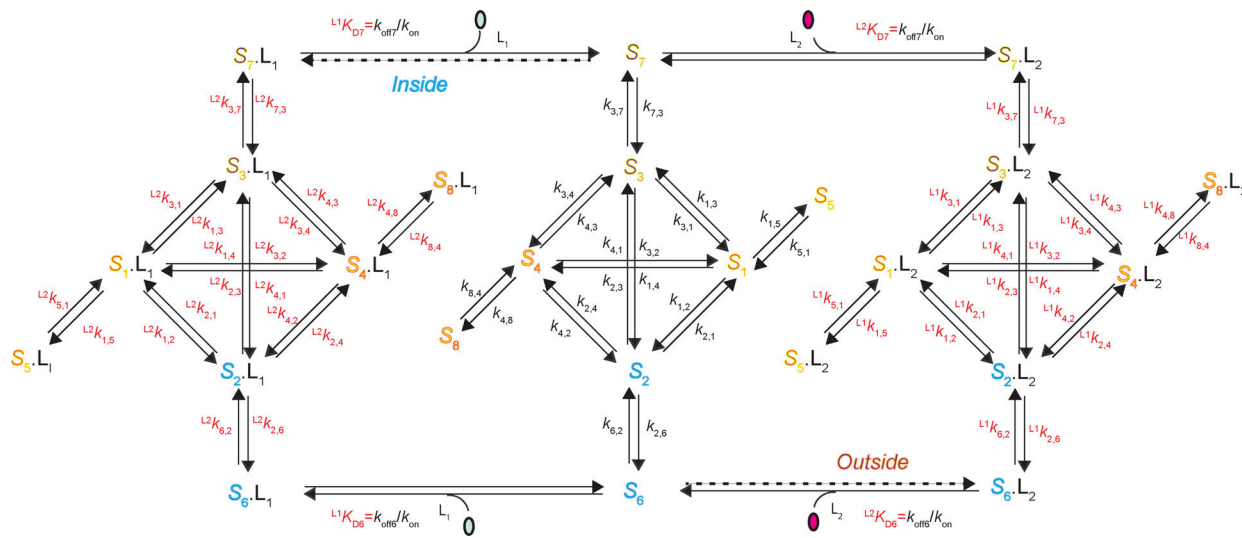


Figure 6. A 24-state model of AdiC's conformational kinetics. All states are denoted as described in Results. The middle portion illustrates the transitions of apo AdiC among eight identified states differing in conformation or energy. The left and right portions illustrate the transitions of AdiC bound with two types of ligand, one side for each type. Transition rate constants k_{ij} and $k_{j,i}$, associated with arrows, indicate the reversible transitions between corresponding states i and j (Tables S1, S2, S3, and S4). The transitions directly involving the binding and unbinding of a ligand are labeled with a $K_D = k_{\text{off}}/k_{\text{on}}$.

$$^{app}k_{i,j} = \frac{k_{i,j} + {}^Lk_{i,j} \frac{[L]}{K_{1/2}}}{1 + \frac{[L]}{K_{1/2}}} \quad (3)$$

to all of the plots in Fig. 9, we obtained the rate constants for apo ($k_{i,j}$), Arg⁺-bound, or Agm²⁺-bound AdiC (${}^Lk_{i,j}$), all summarized in Tables S1, S2, S3, and S4. The fits to the Arg⁺ and Agm²⁺ data were coupled to obtain a single set of rate constants for the apo condition.

The first-order rate constant $k_{i,j}$ or ${}^Lk_{i,j}$ corresponds to the mean rate of a molecule to traverse state i to reach state j , without being scaled by p_i . A straightforward way to obtain $k_{i,j}$ and ${}^Lk_{i,j}$ is to collect the data under the condition that both sides of AdiC are exposed to the same series of substrate concentrations such that $k_{i,j}$ and ${}^Lk_{i,j}$ can be estimated by extrapolating to the zero and saturating-ligand concentrations, respectively. Here, satisfying this condition, both sides of individual AdiC molecules, each in a nanodisc, faced the same series of solutions. Under the apo, Arg⁺-bound, or Agm²⁺-bound condition, $k_{1,5}$, $k_{2,6}$, $k_{3,7}$, or $k_{4,8}$ are markedly slower than the other rate constants, seen in Fig. S4 as taller columns that represent the inverse values of rate constants. Among them, $k_{2,6}$ and $k_{3,7}$ quantitatively define the transitions on the transport pathway, each of which immediately precedes an actual substrate-releasing step with a much greater rate constant.

Verification of the observed conformational behaviors with a monofunctional fluorophore

Using monofunctional ATTO-550, we tested whether a fluorophore's characteristics affect AdiC's conformational behaviors (Fig. S5). Hydrophobic ATTO-550 is expected to pack itself against hydrophobic local protein elements, but not necessarily along helix 6A. Thus, even if the bifunctional label incidentally affected the conformational changes, a monofunctional label might not act similarly. Without

additional information, the spatial relation between helix 6A and ATTO-550 is unknown. However, if their relation remains statistically constant, the relative orientations of ATTO-550 among the states should report those of helix 6A defined by the local coordinates.

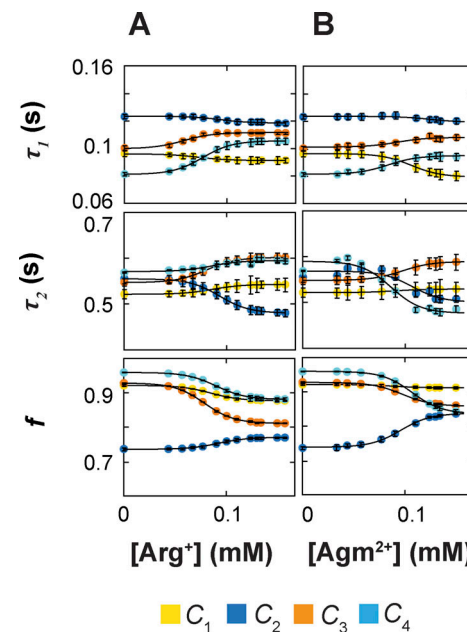


Figure 7. Dependence of exponential fitting parameters on the concentration of ligands. (A and B) Time constants τ_1 and τ_2 of the double-exponential components and the relative amplitude f of the first component plotted against the concentration of Arg^+ (A) or Agm^{2+} (B). All parameters were obtained through double-exponential fits to dwell-time distributions as shown in Fig. 5. All data are presented as mean \pm SEM, and their representing symbols are color coded for states. The curves superimposed on the data are fits of an equation in the same form as Eq. 3. Fitted parameter values are given in Tables S1, S2, S3, and S4.

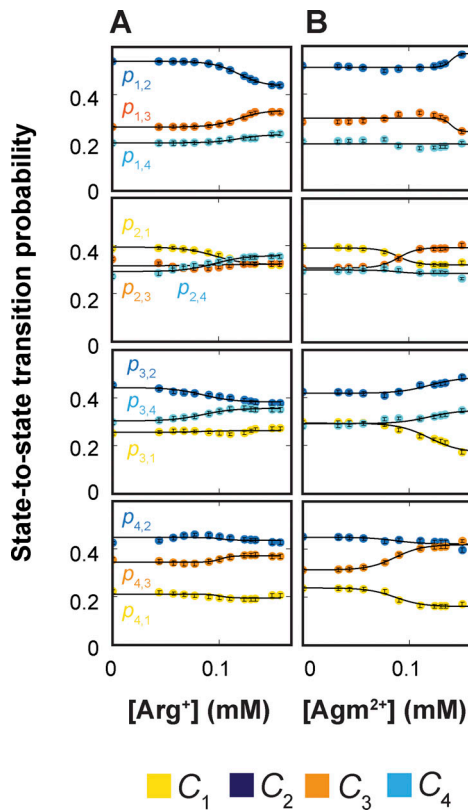


Figure 8. Dependence of probabilities of state-to-state transitions on the concentration of ligands. (A and B) Probabilities of state-to-state transitions plotted against the concentration of Arg⁺ (A) or Agm²⁺ (B). All data are presented as mean \pm SEM, and their representing symbols are color coded for states. The lines superimposed on the data correspond to fits of the respective groups of data to an equation in the same form as Eq. 3. Fitted parameter values are given in Tables S1, S2, S3, and S4.

For all four resolved states, the angles calculated from the intensities of the mono- and bifunctional fluorophores are comparable (Table 1), after corrected for their wobble angles (39.4° versus 27.0°; Material and methods). The mean σ for θ and φ of the monofunctional fluorophore are $3.65^\circ \pm 2.62^\circ$ and $3.64^\circ \pm 2.56^\circ$, compared with $3.73^\circ \pm 2.27^\circ$ and $3.85^\circ \pm 2.48^\circ$ of bifunctional rhodamine. Under the same substrate conditions, the observed probabilities and kinetics of the corresponding states were also comparable for the two compared fluorophore types (Tables S5, S6, S7, S8, and S9).

Determination of the equilibrium constants among the energetics states

To determine all K_D values, we first used Eq. S31 to calculate the probabilities of the eight energetic states S_1 – S_8 (Fig. 10) from the corresponding ${}^{app}k_{i,j}$ values (Fig. 9) for each ligand condition. The resulting values of state probabilities of apo and Arg⁺- or Agm²⁺-bound states are given in Table S10. The K_D values for individual states (Table S11) and those of other equilibrium constants for apo and Arg⁺- or Agm²⁺-bound states (Table S12) were then determined by a global fit to the eight plots for Arg⁺ or Agm²⁺ in Fig. 10 with the following equation:

$$P_i = \frac{K_{i,1} + {}^L K_{i,1} \frac{[L]}{K_D}}{\sum_{i=1}^8 K_{i,1} + \sum_{i=1}^8 {}^L K_{i,1} \frac{[L]}{K_D}} \quad (4)$$

where S_1 is used as a reference for other states (S_i) to define equilibrium constants:

$$K_{i,1} = \frac{[S_i]}{[S_1]}, \quad {}^L K_{i,1} = \frac{[S_i] \cdot L}{[S_1] \cdot L}, \quad K_{Di} = \frac{[S_i] \cdot [L]}{[S_1] \cdot L}, \quad i = 1, 2, \dots, 8 \quad (5)$$

The probabilities of S_6 and S_7 exhibit greater variations with varying ligand concentrations than those of other states, characteristics consistent with S_6 and S_7 being the open states. Thus, K_D for S_6 or S_7 , which characterizes the binding of external or internal ligand Arg⁺ or Agm²⁺, is practically consequential, four of which and the 60 rate constants fully determine the 24-state conformation-kinetic model of AdiC (Fig. 6).

Furthermore, we calculated the relations between the probabilities of C_1 – C_4 and the ligand concentration, each from the corresponding pair of curves fitted to the relevant relations of S_1 – S_8 in Fig. 10, and overlaid them on the observed relations in Fig. 4 A. As expected, the probabilities predicted for the four conformations from the eight energetic states identified by the kinetic analysis match the observed probabilities over the tested ligand concentration range.

Monte Carlo simulation of the time courses of conformational state dynamics

Fig. 11 A exhibits a simulated time course of conformational changes, a type of temporal template used to generate an integrative 4D model of AdiC (Video 2) or to simulate the time-dependent substrate transport (Fig. 11 B). The initial simulated state was designated as S_6 , transitioning to one of the three connected states: S_2 , Arg⁺-bound S_6 or Agm²⁺-bound S_6 after a simulated time (t_{sim}) (Fig. 6). The t_{sim} was obtained by randomly drawing from an exponential distribution of dwell times for S_6 , defined by the rates of exiting to the three states. When the accumulated time became equal to or longer than t_{sim} , AdiC would transition from S_6 to one of the three connected states, which was determined by the outcome of a random draw from a multinomial distribution defined by the three state-to-state transition probabilities (Fig. 8). The t_{sim} of this second state and its termination were determined as described above. These steps were repeated until the end of the simulation.

Characteristics of two alternative 24-state transporter models of opposite sidedness

In the 24 conformational state model, the rate constants of all shown pathways are fully locked in by experimental data. Then, a natural question is whether this model can reasonably predict the observed Michaelis–Menton kinetic behaviors of AdiC, a model analytically expressed in the form of a system of 24 differential equations of no adjustable parameters under a given substrate condition (see supplemental text at the end of the PDF).

The substrate dependence of the rate of Arg⁺ or Agm²⁺ uptake into lipid vesicles embedded with AdiC has previously been examined (Tsai et al., 2012). In their study, the initial concentration of Arg⁺ in the vesicles was always 5 mM, which is a

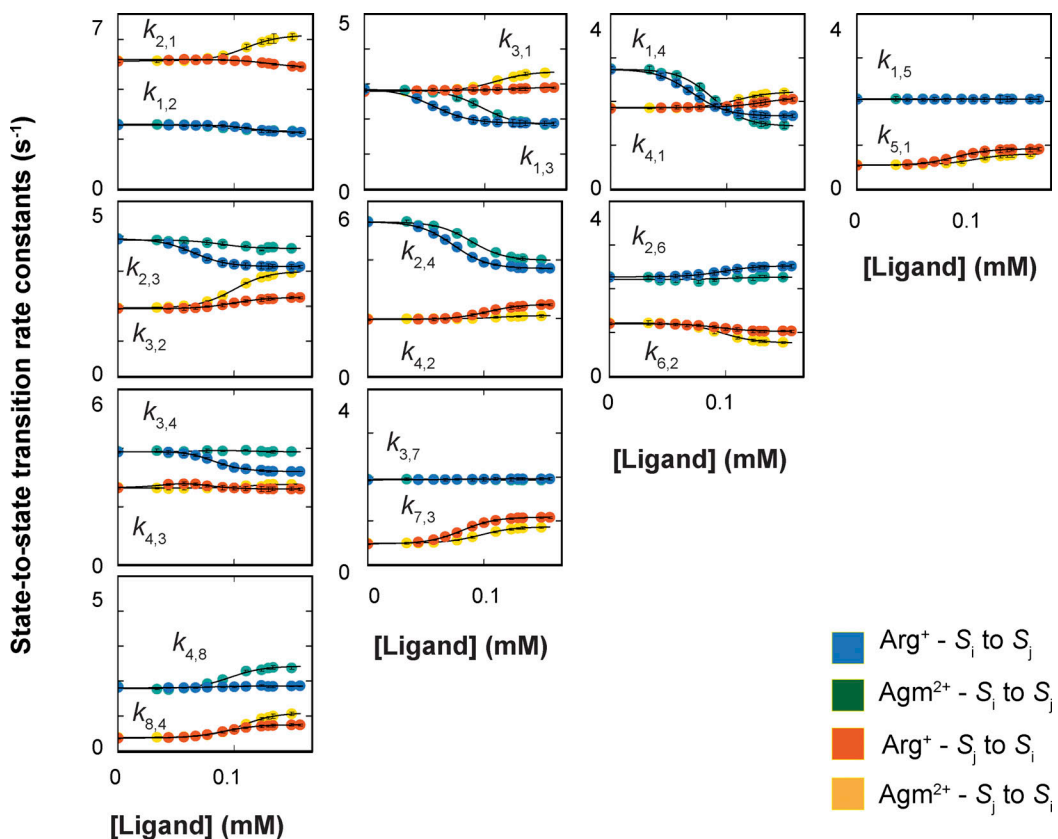


Figure 9. Dependence of apparent state-to-state transition rate constants on the concentration of ligands. Apparent rate constants plotted against the concentration of Arg^+ or Agm^{2+} , obtained as described in Results. All data are presented as mean \pm SEM. The symbols for (forward) or (backward) rate constants, $k_{i,j}$ or $k_{j,i}$, are colored blue or red in the case of Arg^+ , whereas they are colored green or orange in the case of Agm^{2+} . The curves superimposed on the data are fits of an equation with the same form as Eq. 3. Fitted parameter values are given in Tables S1, S2, S3, and S4.

practically saturating concentration, whereas the bathing medium contained a varying initial concentration of radio-labeled Arg^+ and Agm^{2+} . To achieve a directed cysteine-based modification, they replaced native cysteine residues in AdiC, which modestly lowered the apparent transport rate. We also replaced cysteines to avoid off-target labeling. To compare with those functional data, we performed Monte Carlo simulations of the time courses of conformational state dynamics for individually tested conditions (Fig. 11 A), according to the conformation-kinetic model (Fig. 6). In this example, the functionality of conformational states is assigned as shown in Fig. S6. In the simulation, a release of a substrate molecule to the inside occurs during the transition of substrate-bound S_7 to the apo S_7 , whereas a release of a substrate molecule to the outside occurs during the transition of substrate-bound S_6 to apo S_6 . Fig. 11 B exhibits a simulated ~ 30 min time course of the net Arg^+ uptake and the average of those from 100 independent simulations. We also simulated a previously reported ~ 30 min time course of the uptake of radioactive Arg^+ for the initial substrate conditions of 50 μM external radioactive Arg^+ and 5 mM internal nonradioactive Agm^{2+} (Tsai et al., 2012). This simulated time course mimics the observed one in terms of not only the time constant but also the maximum fractional uptake (F_{\max}^{obs}) (Fig. 11 C). Predicting F_{\max}^{obs} by the model with an apo path for the protein-

conformational transitions suggests that AdiC is not an exchanger.

From the observed time course of uptake, Tsai et al. (2012) obtained the relation between the apparent initial uptake rate ($\text{app}k_{\text{flux}}$) and the substrate concentration (Fig. 12, closed dark blue symbols). The relations predicted by the model where C_2 corresponds to E_o and C_3 to I_o , dubbed sidedness configuration 1, is compared with the observed ones in Fig. 12, A–C (the closed red circles), and those by the model where C_2 corresponds to I_o and C_3 to E_o (configuration 2) in Fig. 12, D–F. These two models with opposing sidedness are depicted in Figs. S6 and S7. The predicted relations of the two models are statistically comparable with the observed ones. The mean difference between the predicted and observed values is 1.5 or 1.0 times the mean σ for configuration 1 or 2. Consequently, the values of apparent maximum uptake rate (k_{\max}) and the concentrations (K_m) at half of k_{\max} , which empirically characterize the observed and predicted relations, are also comparable (Table S13). The similar predictions of the two models reflect the nearly symmetric transport-kinetic behaviors in the two directions under the examined conditions (Tsai et al., 2012). While Tsai et al. (2012) performed their study under a condition where a “leak” current dissipated the membrane potential caused by a counter transport of Arg^+ and Agm^{2+} (Fang et al., 2007), we examined AdiC in

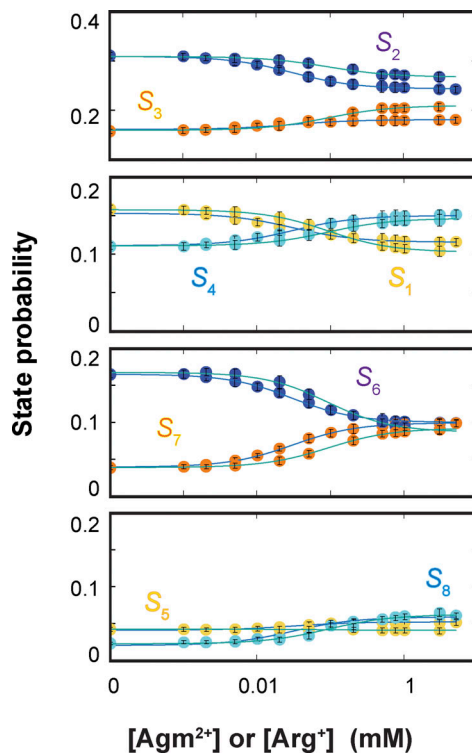


Figure 10. Dependence of probabilities of energetic states on the concentration of ligands. Probabilities of states $S_1 - S_8$ (yellow for S_1 and S_5 ; blue for S_2 and S_6 ; orange for S_3 and S_7 ; and cyan for S_4 and S_8) are plotted against the concentration of Arg^+ (with fitted curves in blue) or Agrm^{2+} (with fitted curves in green). All data are presented as mean \pm SEM. The probability values are calculated using Eq. S31 from the rate constants plotted in Fig. 9. The values for the apo and ligand-bound states are given in Table S10. The curves superimposed on the data are fits of Eq. 4. Fitted parameter values for equilibrium dissociation constants are given in Table S11, and the remaining equilibrium constants in Table S12.

a nanodisc preparation without membrane potential. Thus, we did not consider the membrane potential in either the above Monte Carlo simulations or the following calculations.

A second way to simulate the model-predicted transport characteristics is through direct calculations, using the solutions to the system of 24 differential equations (Eq. S30). One equation corresponds to one state in the 24-state model where the radioactive substrate would be represented by L_E and the non-radioactive substrate by L_I (Figs. S6 and S7). This analytic system is constrained by the 60 determined rate constants for the state-to-state transitions in the model plus four K_D values. Operationally, each K_D needs to be split to the underlying on- and off-rate constants (k_{on} and k_{off}). The association and dissociation of substrate are treated as a rapid equilibrium process. All k_{on} values set to the near diffusion-limited rate $10^7 \text{ M}^{-1} \text{ s}^{-1}$, and k_{off} values, calculated from the respective $k_{on}K_D$, are much larger than other 60 rate constants; none of the calculated k_{off} values limits calculated transporting rates. By these calculations, we directly evaluated the relation between $^{app}k_{\text{flux}}$ and each of the five serially related transitions along the transport path in the model. That is, the transition between S_7 and S_7L , S_7L and S_3L , S_3L and S_2L (whose rate was calculated as the sum of the rates of

three underlying parallel pathways along the direction), S_2L and S_6L , or S_6L and S_6 . Under a given substrate condition, each rate is calculated as the difference between the forward and backward rates of the transition between, e.g., S_2L and S_6L :

$$^{app}k_{\text{flux}} = {}^Lk_{2,6} {}^LP_2(L) - {}^Lk_{6,2} {}^LP_6(L) \quad (6)$$

For a given condition, the rate was calculated using time-dependent substrate concentrations and state probabilities (see supplemental text at the end of the PDF). As such, both the changes in the concentrations of a given substrate species and the changes in probabilities of individual states in response to the changing substrate concentrations were taken into consideration.

For a given AdiC orientation and specific substrate conditions, the calculated relation between $^{app}k_{\text{flux}}$ and the substrate concentration is the same for the five transitions and very similar to the corresponding one obtained in the above Monte Carlo simulation (Fig. 12; a set of concentric circles versus the corresponding closed red circles). As such, the flux rate across the system in the direction of transport is essentially uniform and can be approximated by that of each of those transitions. Thus, following a perturbation caused by a change in the substrate concentration, the conformation-energetic states of AdiC themselves reach a new (near) equilibrium state within a timeframe much shorter than the process of the net transfer of a single substrate molecule. Such a characteristic is expected for the case where the forward and backward rates of individual transitions are comparable, and the net flux rate reflects the difference between the rates in two opposite directions.

If the flux rate can be estimated from a single transition, one may wonder what the importance of the information regarding all the remaining states is. This importance stems from that the apparent transition rate for a state to another state is given by the product of the rate constant and the state probability, and its variation with concentration solely reflects the ligand-dependent variation of the state probability (Eq. 6). Thus, the flux-rate calculation for a given condition requires knowing the probabilities of the two relevant states under that condition, besides their invariant transition-rate constants. The determination of the probabilities of a pair of states in turn requires knowing the probabilities of all remaining states either individually or together, here estimated for a given set of substrate conditions through calculating the time-dependent probabilities of the 24 states from experimentally determined values of rate constants and K_D (see supplemental text at the end of the PDF). What is outlined above highlights the importance to track all states and points to that the occluded cul-de-sac states S_5 and S_8 indirectly affect the transport rate through their probabilities, acting like sinks.

It is noteworthy that the predicted initial rate of transport in the above calculations or Monte Carlo simulations are the true initial rates of the models, whereas the experimental values tend to underestimate initial rates because of low signal-to-background ratio when the substrate concentrations in bathing solution are low and limited time resolution, the latter of which has been shown by Tsai et al. (2012). This issue should, in part,

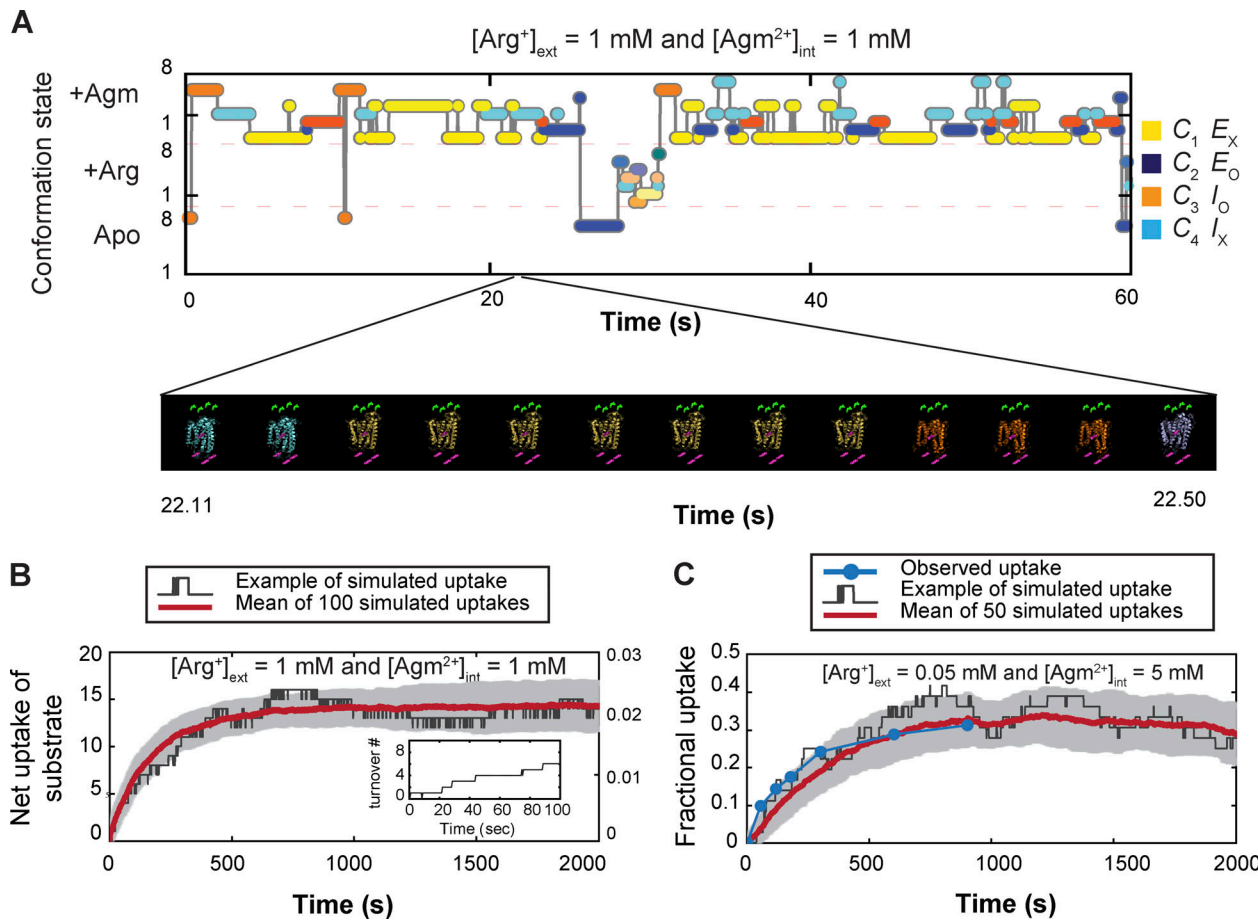


Figure 11. Example of a simulated time course of conformational transitions of AdiC, a segment of a video illustrating a transporter model in 4D, and simulated time courses of net ligand transport. (A) Time course of AdiC transitioning among four types of conformations, simulated with the model shown in Fig. S6 as described in Results for the initial presence of 1 mM extracellular Arg⁺ and 1 mM intracellular Agm²⁺. For distinction, AdiC's presence in the apo, Arg⁺-bound, and Agm²⁺-bound forms are indicated by individual filled circles in the lower, middle, and upper sections of the panel, respectively; its adoptions of C₁ (S₁ + S₅) are colored yellow, C₂ (S₂ and S₆) colored blue, C₃ (S₃ and S₇) colored orange, and C₄ (S₄ and S₈) colored cyan. Shown underneath this simulated time course is a segment from Video 2, exhibiting a 4D model of the transporter proper transitioning among four types of conformations while transporting ligands. The video was generated using the simulated time course shown in the panel A as the temporal template to connect the structures of different states, as described in Results. The shown video frames correspond to the segment of simulated time course from 2,211 to 2,250 ms. **(B)** The time course of uptake of Arg⁺ extracted from the simulation shown in panel A. The black trace illustrates the time course yielded from a simulation of a single subunit of AdiC, where the inset exhibits its first 100 s in an enlarged view. The red trace corresponds to the average of the outcomes from 100 such simulations. **(C)** The observed time course of the fractional net uptake of radioactive Arg⁺ for the initial conditions of 50 μ M external radioactive Arg⁺ and 5 mM internal Agm²⁺ (closed blue circles) (Tsai et al., 2012), overlaid with a single simulated time course (black trace) and the mean of 50 such simulations (red trace). The gray colored zone in panels B or C represents what is defined by mean \pm σ , corresponding to the 68% confidence interval.

underlie the model-predicted rates being nearly equal or modestly greater than the observed rates (Fig. 12).

Additionally, because in the model the transport of each substrate molecule is coupled to AdiC's conformational transitions, the comparability between the model-predicted and observed k_{max} values strongly supports the notion that AdiC is a facilitating transporter rather than a channel, as the latter would allow vastly more than one molecule to pass through it during each adoption of an open conformation. This conceptual distinction is arguably of importance here, given that AdiC does not appear to be an obligatory exchanger but a uniporter.

Regarding the model's sidedness, the above comparison of the models of opposing sidedness with the observed transport behaviors has not been informative because of the relative symmetry at symmetric pH of \sim 5. However, Tsai et al. (2012)

showed that when pH for the extracellular side of AdiC was lowered from 5 to 3, the fractional uptake increased and the ratio of fractional uptakes under these two conditions was less than one. In contrast, when pH for the cytoplasmic side of AdiC was lowered from 5 to 3, the fractional uptake decreased, and the ratio was greater than one. Thus, we further performed the polarization study at pH 3 to determine the individual parameters in our model at this pH. Judging from the opposite effects of lowering pH from 5 to 3, the predictions of the model in configuration 1 but not 2 (Figs. S6 and S7) are consistent with their observations (Fig. 13, A and C versus Fig. 13, B and D).

Macroscopically, a 1:1 exchanger transports equal amounts of substrates in opposite directions. The experimentally observed AdiC-mediated Arg⁺ uptake into bacteria was comparable with Agm²⁺ extrusion and, consequently, the sum of Arg⁺ and Agm²⁺

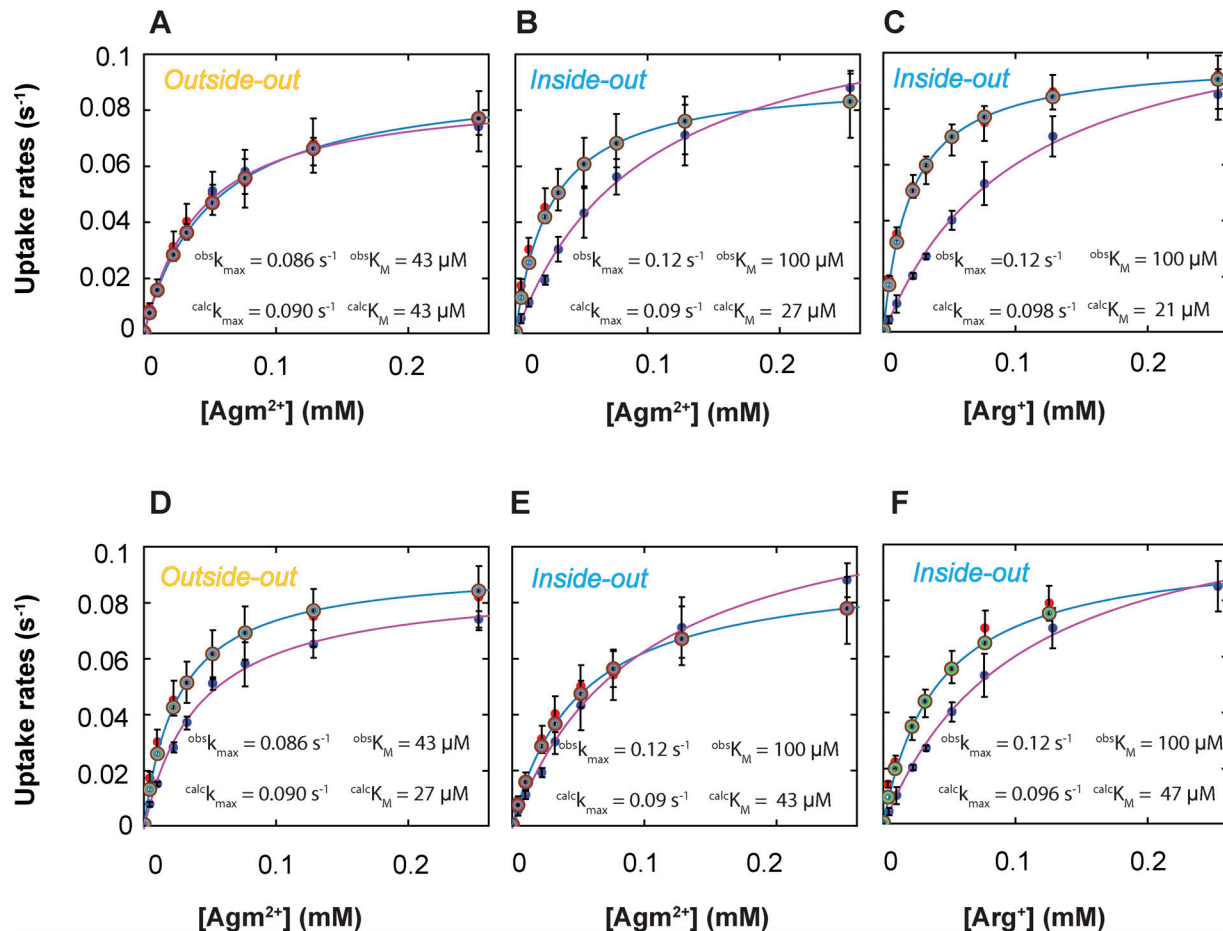


Figure 12. Comparison of observed and model-predicted rates of AdiC-mediated ligand uptakes into lipid vesicles. (A–F) The predicted values by the model shown in Fig. S6 (A–C) or those by the model in Fig. S7 (D–F) are compared with corresponding observed values for a given experimental condition (Tsai et al., 2012). Net ligand uptake rates are plotted against the ligand concentration: Agm^{2+} via AdiC in the outside-out (A and D) or inside-out (B and E) orientation and Arg^+ via AdiC in the inside-out orientation (C and F; see Fig. S9 for the comparison and comments regarding the outside-out orientation). The experimental data are plotted as mean \pm SEM, and the predicted values of the alternative models shown in Figs. S6 and S7 by means of Monte Carlo simulations or calculations are plotted as mean \pm σ calculated from the corresponding confidence interval. The observed data set is represented by closed dark blue circles, the simulated set of the model by closed red circles, and the five calculated sets, one for each transition, by five of practically concentric open circles. The curves, which are superimposed on the symbols that represent the calculated values, correspond to the fits of the Michaelis–Menten equation. All fit parameters of calculated values are presented in Table S13, along with those reported by Tsai et al. (2012). All calculations were performed as described in the supplemental text at the end of the PDF.

in the medium remained arguably constant over time (Iyer et al., 2002). However, these observations were quantitatively simulated using our model of a uniporter, a model that allows AdiC to indirectly transition between E_o and I_o even when it is not bound with any substrate (Fig. 14; see supplemental text). The observations likely reflected the experimental conditions of Iyer et al. (2002), under which the substrate concentrations on both sides of the bacterial membrane were sufficiently high such that the probabilities of the apo states were minimized. Thus, the results of Iyer et al. (2002) are necessary but insufficient evidence for AdiC being an obligatory 1:1 exchanger instead of a uniporter.

Furthermore, Iyer et al. (2003) examined the dependence of the Agm^{2+} -efflux rate from bacteria on the Arg^+ concentration in the medium. For clarity, we replotted their observed rate values against the Arg^+ concentration on a logarithmic scale (Fig. S8). The simulations of our model generally match their data (closed

blue circles versus green squares), except for the rate at the highest tested Arg^+ concentration, which is lower than that at a lesser concentration and thus most likely reflects an experimental error. These simulations show the trajectory expected for a uniporter, i.e., the efflux rate approaches a nonzero minimum as the external substrate concentration is lowered toward zero. However, after eliminating the apo pathway for the conformational changes to mimic an exchanger, the model failed to predict the data of Iyer et al. (closed red circles versus green squares), while exhibiting a key characteristic of exchangers, i.e., the efflux rate approaches zero as the external substrate concentration is lowered toward zero.

Radioactive substrate flux assays to test the transport model with an apo pathway for conformational transitions

If the observed transitions of AdiC among the apo states are genuine and not caused by such experimental factors as the

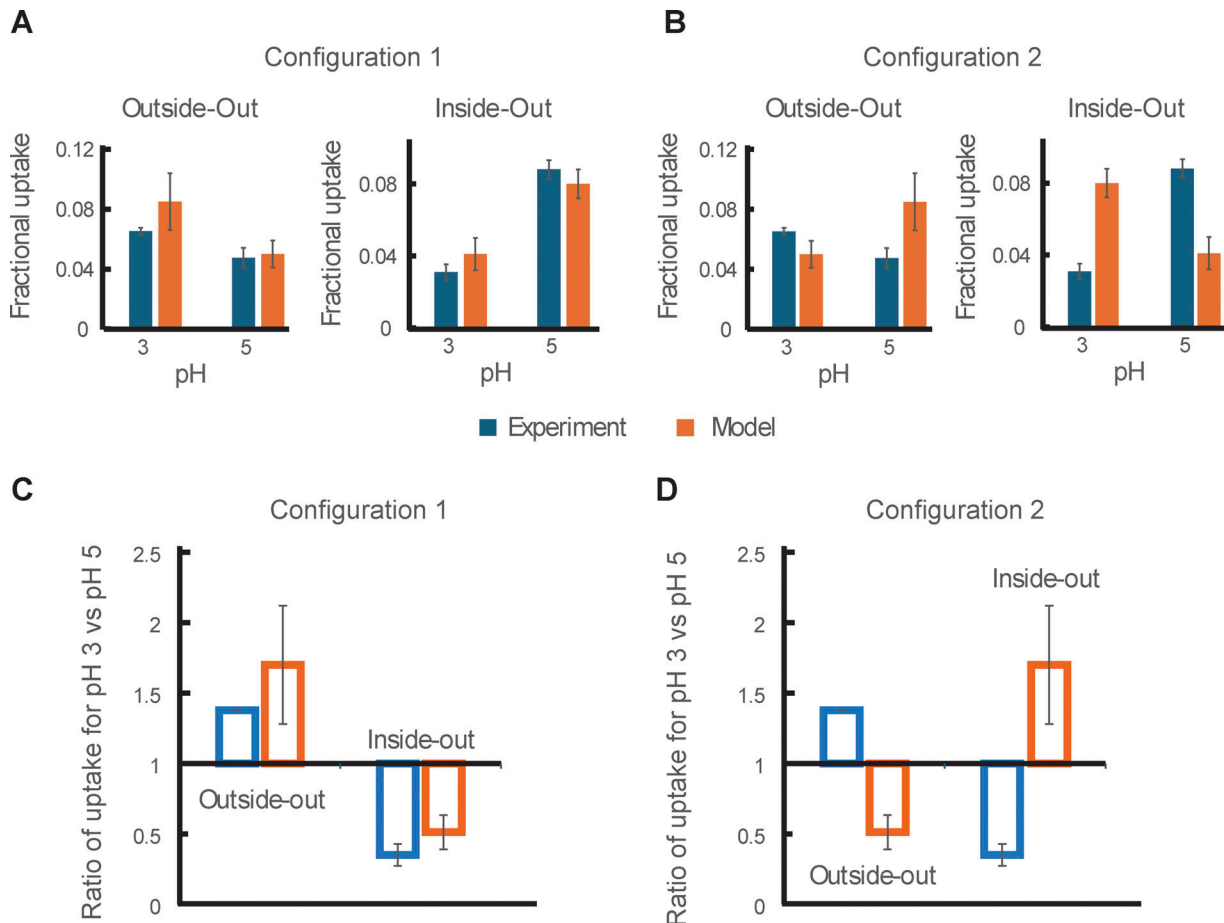


Figure 13. Simulations of the pH-dependent uptake of Arg⁺ under asymmetric conditions using our model in two configurations of opposite sidedness. (A and B) Fractional uptake values (mean \pm SEM) were previously reported by Tsai et al. (2012), which were obtained via assaying radioactive Arg⁺ fluxes into vesicles with AdiC reconstituted in the outside-out or inside-out orientation (closed blue bars). As initial conditions, the solution of pH 5 in vesicles contained 5 mM Arg⁺, whereas the bathing solution of pH 3 or pH 5 contained 50 μ M of radioactive Arg⁺. The fractional uptake values were determined 5 min after the initiation of the experiments. We simulated their data using our model in the configurations 1 (A) and 2 (B) of opposite sidedness illustrated in Figs. S6 and S7, respectively (closed orange bars; mean \pm σ). The kinetic parameters for the two different sides of the model were those determined in the corresponding pH conditions. (C and D) The ratios between the experimental values for pH 3 and pH 5 in the outside or inside-out orientation (open blue bars) compared with those predicted by the model in configuration 1 (C) and 2 (D) (open orange bars).

fluorophore label, unlabeled AdiC should not act as an exchanger. Thus, we examined this prediction using traditional radioactive uptake assays.

The uptake of radioactive substrate via exchangers into vesicles can be rationalized using a simple thermodynamic system of two compartments connected via a 1:1 substrate exchange, without any meaningful interactions with the environment during the considered timeframe. At the time $t = 0$, the internal (i) compartment, representing all vesicles together, contains nonradioactive substrate (NR) of the concentration $[NR_i](0)$, whereas the external (e) compartment, representing the external bathing solution, harbors radioactive substrate (R) of the concentration $[R_e](0)$. A substrate exchange between the two compartments merely allows substrate molecules in them to move and mix. Necessitated by the law of mass conservation, an exchange-based mixing process cannot alter the combined number of substrate molecules or concentration of different substrate types in either compartment. Furthermore, the second law of thermodynamics necessitates the maximization of the

system's entropy when equilibrium is reached at $t = \infty$, such that the probability (p^R) to pick out an R from either compartment should be the same:

$$p_i^R = \frac{n_i^R(\infty)}{n_i^R(\infty) + n_i^{NR}(\infty)} = \frac{1}{1 + \frac{n_i^{NR}(\infty)}{n_i^R(\infty)}} \quad (7)$$

and

$$p_e^R = \frac{n_e^R(\infty)}{n_e^R(\infty) + n_e^{NR}(\infty)} = \frac{1}{1 + \frac{n_e^{NR}(\infty)}{n_e^R(\infty)}} \quad (8)$$

where n^R or n^{NR} denotes the number of R or NR. The equality between Eqs. 7 and 8 leads to

$$\frac{n_e^{NR}(\infty)}{n_e^R(\infty)} = \frac{n_i^{NR}(\infty)}{n_i^R(\infty)} = \frac{n_e^{NR}(\infty) + n_i^{NR}(\infty)}{n_e^R(\infty) + n_i^R(\infty)} = \frac{n_i^{NR}(0)}{n_e^R(0)} \quad (9)$$

Under these conditions, the maximal fractional uptake (F_{max}) is expressed as

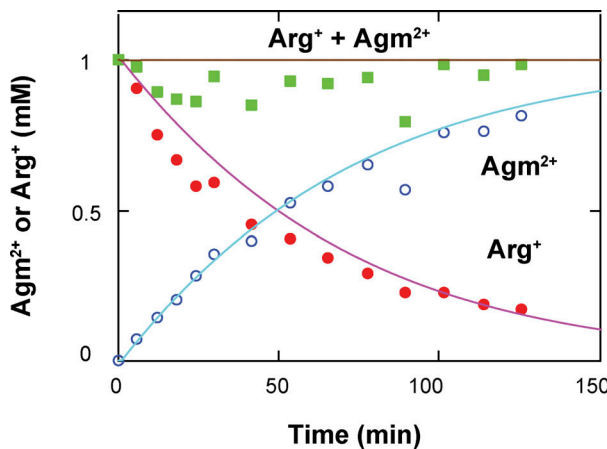


Figure 14. Comparison of observed and model-predicted rates of substrate transport across bacterial membranes. The observed concentration of Arg⁺ (red closed circles), Argm²⁺ (blue open circles), or their sum (green squares) in the bacteria culture medium plotted against observation time (Iyer et al., 2002). The curves overlaid on the experimental data represent the calculated Arg⁺ (magenta) and Argm²⁺ (blue) concentrations with the model depicted in Fig. S6. The brown line on top corresponds to the sum of the calculated Arg⁺ and Argm²⁺ concentrations. All calculations were performed as described in the supplemental text at the end of the PDF.

$$F_{max} = \frac{n_i^R(\infty)}{n_e^R(0)} = \frac{1}{1 + \frac{n_e^R(0)}{n_i^{NR}(0)}} = \frac{1}{1 + \frac{[R_e](0)V_e}{[NR_i](0)V_i}} = \frac{1}{1 + \frac{r_v}{r_c}} \quad (10)$$

F_{max} and the first three ratios in Eq. 9 all describe the outcomes of the equilibrating process of radioactive substrate being partitioned between the bathing solution and vesicles via a 1:1 exchange. Consistent with not only theory but also intuition, these outcomes are predetermined by $\frac{n_e^R(0)}{n_i^{NR}(0)}$ or $\frac{r_v}{r_c}$. Thus, after the accumulation of radioactive substrate in the vesicles reaches the maximum, this maximal level should persist until the substrate condition is altered.

To test this prediction for a 1:1 exchanger, we focused on examining the sustainability of the maximum accumulation, over a period of 3 or 4 h following initiation of the uptake process, which was much longer than 2.5–30 min in previous studies (Fang et al., 2007; Tsai et al., 2012; Tsai and Miller, 2013). We first examined the wild-type AdiC protein, allowing the maximal accumulation of radioactive Arg⁺ in the vesicles under the conditions of $[NR_i](0) = 50$ mM and $[R_e](0) = 0.5$ mM. The fractional uptake remained practically constant over 3 h (Fig. 15 A). While this finding is consistent with AdiC being an exchanger, it could also reflect the behavior of a transporter with an apo pathway for conformational changes, such as a uniporter, that acted like an apparent exchanger when the starting substrate concentrations on both sides of the vesicle membranes were much higher than the respective K_D values such that the utilization of the apo pathway would be negligible. For a genuine exchanger, the fractional uptake should remain constant over time, even if we repeated the study with a much lower starting substrate concentration of the bathing solution. By contrast, for a uniporter, a drop of the fractional uptake might be observed over an adequately long observation period if the starting substrate concentration were sufficiently low. Thus, we lowered the

starting concentration of the bathing solution from 0.5 mM to 50 μ M and found that the fractional uptake dropped modestly over 4 h. This drop should not reflect a non-AdiC-mediated leak of vesicles because it only occurred when the bathing solution initially contained a low (50 μ M) but not a saturating high concentration (0.5 mM) of Arg⁺. Next, we repeated the study with the mutant AdiC protein used in our polarization study under the conditions of $[NR_i](0) = 50$ mM and $[R_e](0) = 50$ μ M, the latter of which is comparable with the observed or model-predicted K_m values (Figs. 12 and S9). The level of accumulation of radioactive substrate via the mutant AdiC also dropped with time (Fig. 15 B). This drop should primarily reflect a net efflux of both radioactive and nonradioactive substrates along the concentration gradient in the presence of an apo path for the conformational transitions, as the full mixing of radioactive and nonradioactive species would largely be completed near the peak. Our kinetic model of the AdiC transport with all parameters fixed by the polarization data predicts the declining time course observed with the same AdiC mutant used in the polarization study (Fig. 15 B). It also predicts that the maximum drop would occur over >40 h (Fig. 15 B, inset).

Ultimately, we must quantitatively evaluate F_{max}^{obs} in a thermodynamically predictable manner, analogous to the evaluation of a channel's ion selectivity. This selectivity is commonly evaluated by comparing the reversal potential on the transmembrane ion-concentration gradient to the prediction of the Nernst equation. Here, to further determine whether AdiC is an obligatory exchanger, we examined F_{max}^{obs} against expected F_{max} under various substrate conditions. The equilibrium quantity F_{max} , by means of a 1:1 exchanger, is a function of $\frac{r_v}{r_c}$ (Eq. 10). Thus, as a prerequisite for calculating F_{max} at a specific r_c , r_v needs to be determined (Eq. 10). For both exchangers or uniporters, under the symmetric concentration condition of $[NR_i](0) = [R_e](0)$ or $r_c = 1$, r_v can be calculated as

$$r_v = \frac{1 - F_{max}^{obs}}{F_{max}^{obs}} \quad (11)$$

For the condition of $[NR_i](0) = [R_e](0) = 50$ mM, we determined r_v as 129 ± 8 or 110 ± 7 for wild-type or mutant preparations (see Materials and methods) and used them to calculate the expected F_{max} values for comparison with those observed in the following studies.

Fig. 15, C and D, shows the relation between the fractional uptake via the wild-type or mutant AdiC at the end of 4 h ($F_{4\text{ h}}$), observed under the conditions that the initial concentration of radioactive Arg⁺ in the bathing solution was varied over a 5 log-unit range, whereas the initial concentration of nonradioactive Arg⁺ in vesicles was always 50 mM. As expected, the fractional uptake was higher when the starting Arg⁺ concentration in the bathing solution was lower. If AdiC were an exchanger and could therefore maintain the F_{max} , $F_{4\text{ h}}$ should match the predicted F_{max} for a given condition (Eq. 10). However, $F_{4\text{ h}}$ diverges from the predicted F_{max} as the Arg⁺ concentration in the bathing solution was lowered, a behavior incompatible with an exchanger but a uniporter. Our model with the parameters fixed by the polarization data obtained with an AdiC mutant agrees with the radioactive flux data of the same mutant (Fig. 15 D).

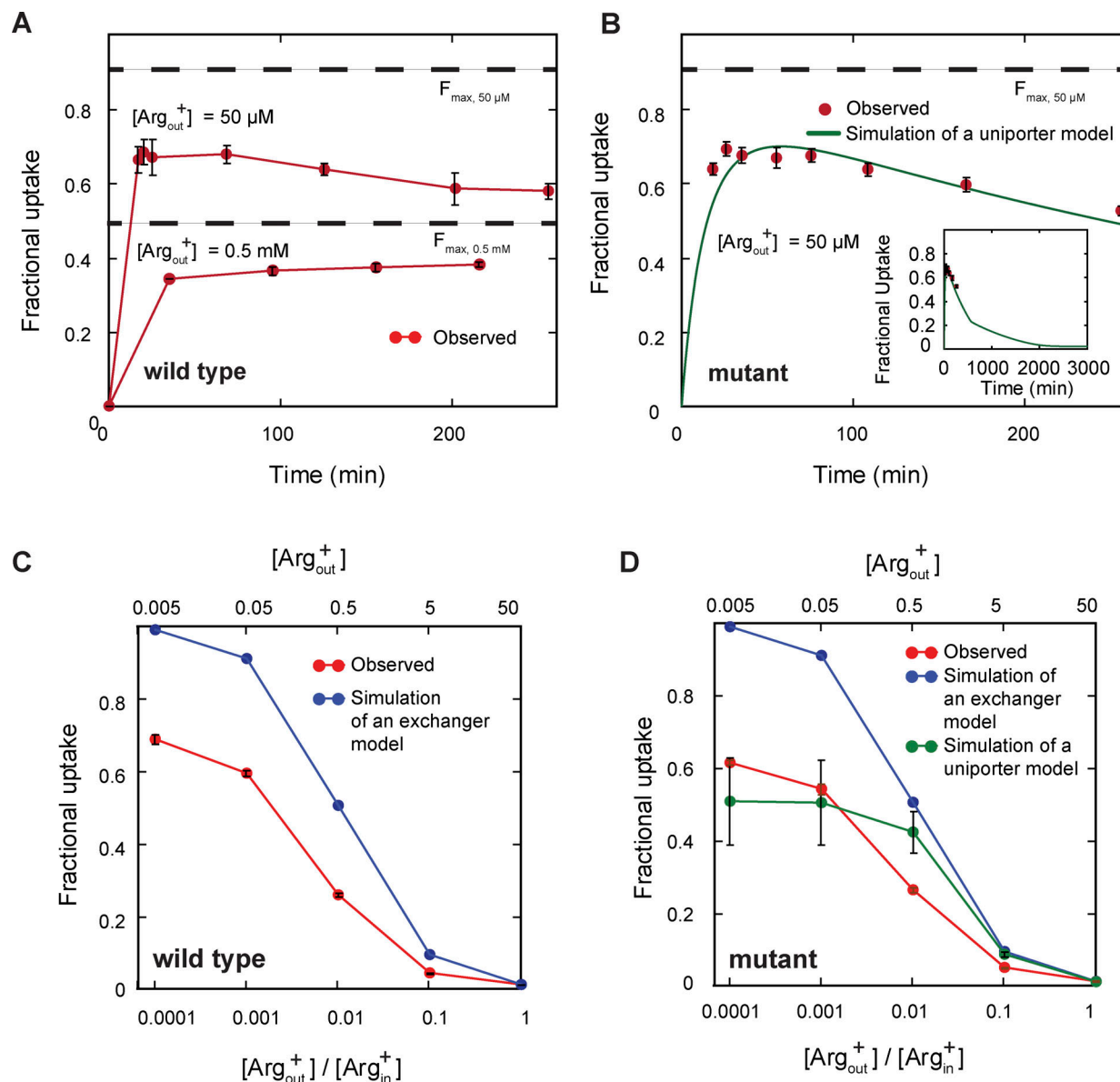


Figure 15. Radioactive flux assays of wild-type and mutant AdiC. **(A and B)** Time courses of radioactive Arg⁺ uptake from the bathing solution into the lipid vesicles embedded with the wild-type (A) and the mutant (B) AdiC molecules. The initial concentration of nonradioactive Arg⁺ inside the vesicles was 50 mM in all cases. At the time $t = 0$, radioactive Arg⁺ at a concentration 0.5 mM or 50 μM in A and 50 μM in B were added to the bathing solution to initiate the transport process. The graph in B is plotted for a >10-fold longer period in the inset. Data points are presented as fractional uptakes (mean \pm SEM), defined as radioactive Arg⁺ inside the vesicles as a fraction of the total radioactive Arg⁺ in the sample. The number of assays were 3–6, except 2 for the leftmost data point for the 0.5 mM condition in A. The black dashed lines indicated the theoretically maximum fractional uptake expected for a 1:1 exchanger under the corresponding conditions. The smooth curve (green) overlaid on the data in B is calculated with the model, as described in Results and in Supplemental material. Given the sidedness of AdiC is random in the vesicle, the average of simulations with two models in Figs. S6 and S7 is plotted, labeled as simulation of a uniporter model. **(C and D)** Uptake of radioactive Arg⁺ with different initial Arg⁺ concentrations in the bathing solution while the initial concentration of nonradioactive Arg⁺ in the vesicles was always 50 mM. The fractional uptakes (mean \pm SEM; $n = 3$) via the wild-type (C) or the mutant (D) AdiC molecules at $t = 4$ h are represented by red dots, plotted against the concentration of Arg⁺ in the bathing solution (upper x axis) or against the ratio of initial Arg⁺ concentrations in the bathing solution and in the vesicles (lower x axis). The blue dots are the theoretical maximum uptake predicted for a 1:1 exchanger under the corresponding substrate conditions. The green dots in D represent the fractional uptakes (mean \pm SEM) simulated by means of a Monte Carlo method, using our model with an apo path for conformational transitions, which is labeled as simulation of a uniporter model, as described above. An equal ratio of the two configurations of the model was used in all simulations to mimic the random insertions of AdiC in the two opposite membrane orientations in the flux assays.

Downloaded from https://jgp.jnlnls.org/jgp/article-pdf/115/1/3/202413709/1393288.pdf - 2024-02-09 09:00:00 by guest on 09 February 2024

A similar phenomenon was found by analyzing data of Fang et al. (2007). In their experiments, $F_{\text{max}}^{\text{obs}}$ was about 0.5 or 0.3 under the conditions that the estimated r_v was about 50; the initial radioactive Arg⁺ in the bathing solution was 50 μM and

nonradioactive Agm^{2+} or Arg⁺ in the vesicles was 5 mM; a leak current dissipated the membrane potential. The $F_{\text{max}}^{\text{obs}}$ value for the Agm^{2+} or Arg⁺ condition is indicated by the blue or green line in Fig. S10 A, both of which are markedly below the

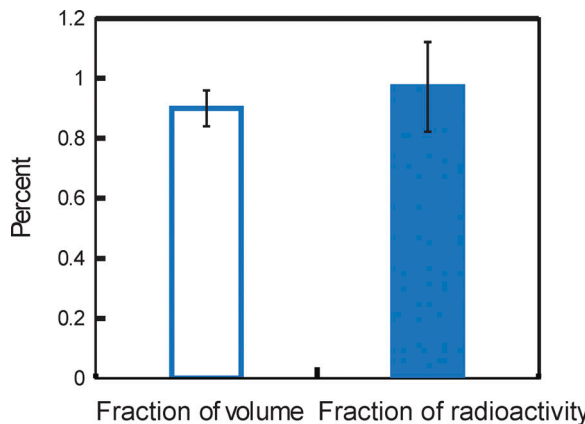


Figure 16. Comparison between the fractions of volume and radioactivity of vesicles. The fraction of volume of vesicles as a percentage of the total reaction volume (mean \pm SEM; $n = 3$) and that of radioactivity in the vesicles as a percentage of total radioactivity ($n = 6$) determined 2.5 h after initiation of the experiment are plotted as an open bar and a closed bar, respectively. At the beginning of experiment, the vesicles were free of substrate, whereas the bathing solution contained 2 mM radioactive Arg⁺.

theoretical F_{max} of 0.67 (black dashed line). By contrast, our model-predicted F_{max} reasonably agrees with F_{max}^{obs} with about 1σ separation; closed blue or green circles represent the simulated values for the presence of 5 mM Arg⁺ or Agm²⁺ in the vesicles. Furthermore, after eliminating the apo path for conformational changes in our model, the resulting exchanger model predicted the fractional uptake to approach the theoretical F_{max} (Fig. S10 B, open black and maroon open squares versus the dashed line). Additionally, our model also predicts a substrate-dependent efflux from vesicles (Fig. S11 A), a phenomenon previously shown by Fang et al. (2007).

Absent any transportable substrate in the vesicles, exchangers cause no uptake beyond their single turnover. By comparison, for a uniporter, radioactive Arg⁺ should be partitioned between the bathing solution and vesicles simply according to their volume ratio at equilibrium. The fractional uptake would be given by $\frac{1}{1+r_v}$ because the concentrations of radioactive Arg⁺ should become the same on both sides of the membrane. Calculated from $r_v = 110 \pm 7$ of the mutant AdiC, the fractional volume of all vesicles was $0.90\% \pm 0.06\%$. This fractional volume statistically matches the fractional uptake of $0.97\% \pm 0.15\%$ ($n = 6$) at 2.5 h from the start of the assay when the vesicle contained no substrate, a match expected for a uniporter (Fig. 16). Similarly, Fang et al. (2007) reported an ~ 0.02 fractional uptake at ~ 30 min when the vesicle contained nonfunctional D-Arg⁺ (the black line in Fig. S10 A). This fractional uptake of ~ 0.02 (above the control taken as being obtained using AdiC-free vesicles) also matches the estimated vesicles' fractional volume of ~ 0.02 . Our uniporter model predicts a fractional uptake of 0.02 under their conditions (closed black diamonds in Fig. S10 A).

Additional evidence contradicting the exchanger hypothesis is an increase in F_{max}^{obs} with lowering pH symmetrically on both sides of the membrane in the presence of a leak current dissipating the membrane potential (Fang et al., 2007). A similar

trend was subsequently shown with a mutant AdiC when the substrate on either side of membrane was Arg⁺ (Tsai et al., 2012). F_{max} of an obligatory 1:1 exchange is thermodynamically predetermined by the initial condition $\frac{n^{NR}(0)}{n^R(0)}$ or $\frac{r_v}{r_c}$ (Eq. 10) and should thus be independent of such a kinetics-influencing factor as pH. However, the rate to reach F_{max} depends on the kinetics and thus pH. Our model predicts an increase in the maximal peak fractional uptake with lowering pH (Fig. S11 B). Following the elimination of the apo path for conformational transitions, the model predicts the fractional uptake to approach the F_{max} predicted for a 1:1 exchanger, independent of pH (inset, Fig. S11 B).

An integrative 4D model of AdiC

To create an integrated 4D transporter model for a chosen ligand condition, we used the temporal template shown in Fig. 11 A to connect the existing experiment-based structural models of individual conformational states. This 4D model is defined by: (1) the experiment-constrained 24-state kinetic model documented by the state diagram (Figs. 6 and S6), analytically expressed by the solutions to a system of 24 differential equations (Eq. S30) and fully defined by 60 $k_{i,j}$ (Tables S1, S2, S3, and S4) plus 4 K_{di} (Table S11); (2) the crystal structure models of the E_O and E_X states of an AdiC monomer (PDB 7O82 and 3L1L) and those of the I_O and I_X states of BasC and ApcT proper (PDB 6F2G and 3GIA) as AdiC's proxies; and (3) the state-specific orientation information of helix-6A that directly links the corresponding structural and conformational states. To effectively exhibit the transporter model, we generated a video to illustrate the dynamic characteristics of conformational mechanism underlying the counter transport of Arg⁺ and Agm²⁺ (Video 2 for viewing in a small window). 13 frames of such a video are shown in Fig. 11 A. This integrative 4D model summarizes our collective understanding of the conformational dynamic mechanism underlying substrate transport in both spatial and temporal dimensions.

Discussion

Our primary goals are to use AdiC as an example to demonstrate: (1) how to use the present microscopy method to determine a very large number of parameters that fully quantify a protein's complex conformational behaviors in the temporal domain and (2) how to extract the underlying kinetic rate constants and equilibrium dissociation constants from these parameters, with which we can establish a model that quantitatively accounts for the observed conformational dynamics. These demonstrations have led to the determination of the 60 rate constants and 4 equilibrium dissociation constants that fully define a 24-state kinetic model of AdiC, whose analytic solution is derived in the supplemental text at the end of the PDF (Fig. 6; see also Fig. S12). The successful determination of such a complex conformation-kinetic mechanism of AdiC demonstrates the unprecedented resolving power of the present method.

The conformation-kinetic model is built from the polarization data, not optimized for its ability to describe transport-functional characteristics. However, given that a protein's structural conformations are the physical determinants of its function, an adequate knowledge of its conformational kinetics

should predict its function. Indeed, our conformation-kinetic model satisfactorily predicts relevant previous and present functional data of AdiC (Figs. 11 C, 12, 13, 14, 15, 16, S8, S9, S10, and S11).

Mechanistically, the present study reveals AdiC's complex kinetics of transitioning among eight inherent states differing in conformation or free energy. These transitions occur spontaneously, depending on thermal energy. They enable AdiC to facilitate the transmembrane movement of Arg⁺ or Agm²⁺ and thus exhibit the substrate-concentration dependence. The concentration gradient of either Arg⁺ or Agm²⁺ or both would perturb the inherent probabilities of individual states (Eq. S32), altering the net transmembrane flux of substrate (Fig. 15).

The unexpected observation of AdiC transitioning among all resolved conformations bound with or without substrate is inconsistent with AdiC being an exchanger. To corroborate this finding, we performed radioactive flux assays and found: (1) AdiC-containing vesicles could hold a maximum uptake of radioactive substrate over several hours, only when the starting substrates concentration on both sides of vesicle membrane were much higher than K_D values; (2) the fractional uptake of radioactive substrate dropped over a long observation period, if the starting concentration of substrate in the bathing solution was lowered to near K_m values; and (3) under low substrate conditions, the observed fractional uptakes at $t = 4$ h were markedly lower than the theoretical F_{max} values predicted for a 1:1 exchanger but are generally predicted by our model (Fig. 15). As outlined in Results, our experimental findings and uniporter model are consistent with the relevant previous studies, all of which are incompatible with AdiC being a 1:1 exchanger. Nonetheless, with sufficiently high concentrations of substrates on both sides of the vesicle membrane, the utilization of the apo pathway for conformational changes in AdiC should be minimized, a condition that would cause AdiC to act like an exchanger (Fig. 14 and Fig. 15 A).

Biologically, enterobacteria acquire environmental Arg⁺ via several transporters (Charlier and Bervoets, 2019). In bacteria, Arg⁺ is decarboxylated, yielding Agm²⁺ and CO₂. Eliminating CO₂ lowers cytosolic acidity. If AdiC is a uniporter, it will facilitate the extrusion of excess Agm²⁺ converted from Arg⁺ acquired via multiple types of transporters, even when the environmental Arg⁺ concentration is low. Extrusion of divalent Agm²⁺ against the strongly negative membrane potential of bacteria is even harder than an exchange for a monovalent Arg⁺. To solve this problem, the bacteria resort to the electrical-shunt CLC channels (Iyer et al., 2002).

Motivated by the present study and a general technical need, we compared a monofunctional fluorophore with the standard bifunctional rhodamine and obtained comparable results with them. Attachment of a monofunctional fluorophore requires only a single cysteine, enabling the use of even a suitable native cysteine. The large collection of commercially available monofunctional fluorophores of various beneficial features may now be utilized, features including high quantum yield, long photo-bleaching time at a given excitation intensity, and different emission wavelengths. As such, multiple domains in a protein

molecule can be tracked by labeling them with multiple fluorophores of different colors.

In summary, using the AdiC transporter, we have demonstrated the unprecedented capability of a high-resolution fluorescence polarization microscopy system in acquiring the data required for solving a highly complex kinetic mechanism of transmembrane protein conformational dynamics. The acquisition of these data and their subsequent analysis have led to the determinations of 60 rate constants and 4 equilibrium dissociation constants. These determinations enabled us to establish an analytic conformation-kinetic model of 24 states expressed by a system of 24 differential equations that is fully constrained by the polarization data and can be used to qualitatively account for the conformational behaviors of AdiC for a given set of specific substrate conditions. This conformation-kinetic model, which has no adjustable parameters for a given substrate condition and pH, also satisfactorily predicts the previous and present observations of AdiC's transport behaviors, even though the model building was uninfluenced by these transport behaviors. The transitions among all resolved conformations in the absence of substrates, which are detected from the polarization measurements, and the data yielded from previous relavent or present flux assays are all incompatible with the prevailing hypothesis that AdiC is a 1:1 exchanger. Here, the temporal information acquired in the polarization study is essential for our understanding the mechanisms of AdiC in 4D as well. Combining this temporal information and the existing structural information, we have illustrated how to construct an experiment-based integrative 4D model to capture and exhibit the spatiotemporal mechanisms of a facilitated transport of an amino acid and its metabolite. Thus, a combination of the present method and existing structural techniques serves as an effective means to help transition structural biology, including crystallography and cryo-EM, which has thus far been highly successful in the characterization of individual static structures, to an integrative form of dynamic structural biology. In addition, as a technical advance, we have successfully showcased the use of a monofunctional fluorophore in the present type of polarization microscopy study. Here, this monofunctional fluorophore and the standard bifunctional rhodamine yielded statistically comparable information, in terms of the number of resolvable conformational states and their relative orientations, probabilities, or kinetics. A use of monofunctional fluorophore will make the present method of an unprecedented kinetics-resolving capability more readily applied to the investigation of the conformational dynamics of many other types of protein.

Data availability

The data used in the present study are available upon reasonable request.

Acknowledgments

Olaf S. Andersen served as editor.

This study was supported by the grant DK125521 from the National Institute of Diabetes and Digestive and Kidney Diseases.

Author contributions: J.H. Lewis: conceptualization, data curation, formal analysis, investigation, methodology, resources, software, validation, visualization, and writing—review and editing. Y. Zhou: conceptualization, formal analysis, investigation, methodology, visualization, and writing—original draft. Z. Lu: conceptualization, funding acquisition, project administration, supervision, and writing—original draft, review, and editing.

Disclosures: The authors declare no competing interests exist.

Submitted: 22 October 2024

Revised: 19 December 2024

Accepted: 19 January 2025

References

Adachi, K., R. Yasuda, H. Noji, H. Itoh, Y. Harada, M. Yoshida, and K. Kinosita Jr. 2000. Stepping rotation of F1-ATPase visualized through angle-resolved single-fluorophore imaging. *Proc. Natl. Acad. Sci. USA.* 97: 7243–7247. <https://doi.org/10.1073/pnas.120174297>

Beausang, J.F., H.W. Schroeder III, P.C. Nelson, and Y.E. Goldman. 2008. Twirling of actin by myosins II and V observed via polarized TIRF in a modified gliding assay. *Biophys. J.* 95:5820–5831. <https://doi.org/10.1529/biophysj.108.140319>

Bennett, B.D., E.H. Kimball, M. Gao, R. Osterhout, S.J. Van Dien, and J.D. Rabinowitz. 2009. Absolute metabolite concentrations and implied enzyme active site occupancy in *Escherichia coli*. *Nat. Chem. Biol.* 5: 593–599. <https://doi.org/10.1038/nchembio.186>

Brocchieri, L., and S. Karlin. 2005. Protein length in eukaryotic and prokaryotic proteomes. *Nucleic Acids Res.* 33:3390–3400. <https://doi.org/10.1093/nar/gki615>

Charlier, D., and I. Bervoets. 2019. Regulation of arginine biosynthesis, catabolism and transport in *Escherichia coli*. *Amino Acids.* 51:1103–1127. <https://doi.org/10.1007/s00226-019-02757-8>

Chen, J., and A.K. Gupta. 2001. On change point detection and estimation. *Commun. Stat. Simul. Comput.* 30:665–697. <https://doi.org/10.1081/SAC-100105085>

Corrie, J.E.T., J.S. Craik, and V.R.N. Munasinghe. 1998. A homobifunctional rhodamine for labeling proteins with defined orientations of a fluorophore. *Bioconjug. Chem.* 9:160–167. <https://doi.org/10.1021/bc970174e>

Denisov, I.G., M.A. Schuler, and S.G. Sligar. 2019. Nanodiscs as a new tool to examine lipid–protein interactions. *Methods Mol. Biol.* 2003:645–671. https://doi.org/10.1007/978-1-4939-9512-7_25

Erickson, H.P. 2009. Size and shape of protein molecules at the nanometer level determined by sedimentation, gel filtration, and electron microscopy. *Biol. Proced. Online.* 11:32–51. <https://doi.org/10.1007/s12575-009-9008-x>

Errasti-Murugarren, E., J. Fort, P. Bartoccioni, L. Díaz, E. Pardon, X. Carpéné, M. Espino-Guardi, A. Zorzano, C. Ziegler, J. Steyaert, et al. 2019. L amino acid transporter structure and molecular bases for the asymmetry of substrate interaction. *Nat. Commun.* 10:1807. <https://doi.org/10.1038/s41467-019-09837-z>

Fang, Y., H. Jayaram, T. Shane, L. Kolmakova-Partensky, F. Wu, C. Williams, Y. Xiong, and C. Miller. 2009. Structure of a prokaryotic virtual proton pump at 3.2 Å resolution. *Nature.* 460:1040–1043. <https://doi.org/10.1038/nature08201>

Fang, Y., L. Kolmakova-Partensky, and C. Miller. 2007. A bacterial arginine–agmatine exchange transporter involved in extreme acid resistance. *J. Biol. Chem.* 282:176–182. <https://doi.org/10.1074/jbc.M610075200>

Forkay, J.N., M.E. Quinlan, and Y.E. Goldman. 2000. Protein structural dynamics by single-molecule fluorescence polarization. *Prog. Biophys. Mol. Biol.* 74:1–35. [https://doi.org/10.1016/S0079-6107\(00\)00015-8](https://doi.org/10.1016/S0079-6107(00)00015-8)

Forkay, J.N., M.E. Quinlan, and Y.E. Goldman. 2005. Measurement of single macromolecule orientation by total internal reflection fluorescence polarization microscopy. *Biophys. J.* 89:1261–1271. <https://doi.org/10.1529/biophysj.104.053470>

Forkay, J.N., M.E. Quinlan, M.A. Shaw, J.E. Corrie, and Y.E. Goldman. 2003. Three-dimensional structural dynamics of myosin V by single-molecule fluorescence polarization. *Nature.* 422:399–404. <https://doi.org/10.1038/nature01529>

Foster, J.W. 2004. *Escherichia coli* acid resistance: Tales of an amateur acidophile. *Nat. Rev. Microbiol.* 2:898–907. <https://doi.org/10.1038/nrmicro1021>

Fourkas, J.T. 2001. Rapid determination of the three-dimensional orientation of single molecules. *Opt. Lett.* 26:211–213. <https://doi.org/10.1364/OL.26.000211>

Gao, X., F. Lu, L. Zhou, S. Dang, L. Sun, X. Li, J. Wang, and Y. Shi. 2009. Structure and mechanism of an amino acid antiporter. *Science.* 324: 1565–1568. <https://doi.org/10.1126/science.1173654>

Gao, X., L. Zhou, X. Jiao, F. Lu, C. Yan, X. Zeng, J. Wang, and Y. Shi. 2010. Mechanism of substrate recognition and transport by an amino acid antiporter. *Nature.* 463:828–832. <https://doi.org/10.1038/nature08741>

Gong, S., H. Richard, and J.W. Foster. 2003. YjdE (AdiC) is the arginine:agmatine antiporter essential for arginine-dependent acid resistance in *Escherichia coli*. *J. Bacteriol.* 185:4402–4409. <https://doi.org/10.1128/JB.185.15.4402-4409.2003>

Grinkova, Y.V., I.G. Denisov, and S.G. Sligar. 2010. Engineering extended membrane scaffold proteins for self-assembly of soluble nanoscale lipid bilayers. *Protein Eng. Des. Sel.* 23:843–848. <https://doi.org/10.1093/protein/gzq060>

Guo, A.C., T. Jewison, M. Wilson, Y. Liu, C. Knox, Y. Djoumbou, P. Lo, R. Mandal, R. Krishnamurthy, and D.S. Wishart. 2013. ECMDB: The *E. coli* metabolome database. *Nucleic Acids Res.* 41:D625–D630. <https://doi.org/10.1093/nar/gks992>

Ha, T., J. Glass, T. Enderle, D.S. Chemla, and S. Weiss. 1998. Hindered rotational diffusion and rotational jumps of single molecules. *Phys. Rev. Lett.* 80:2093–2096. <https://doi.org/10.1103/PhysRevLett.80.2093>

Hamana, K. 1996. Distribution of diaminopropane and acetylsperrmidine in Enterobacteriaceae. *Can. J. Microbiol.* 42:107–114. <https://doi.org/10.1139/m96-017>

Ilgü, H., J.M. Jeckelmann, V. Gapsys, Z. Ucurum, B.L. de Groot, and D. Fotiadis. 2016. Insights into the molecular basis for substrate binding and specificity of the wild-type L-arginine/agmatine antiporter AdiC. *Proc. Natl. Acad. Sci. USA.* 113:10358–10363. <https://doi.org/10.1073/pnas.1605442113>

Ilgü, H., J.M. Jeckelmann, D. Kalbermatter, Z. Ucurum, T. Lemmin, and D. Fotiadis. 2021. High-resolution structure of the amino acid transporter AdiC reveals insights into the role of water molecules and networks in oligomerization and substrate binding. *BMC Biol.* 19:179. <https://doi.org/10.1186/s12915-021-01102-4>

Iyer, R., T.M. Iverson, A. Accardi, and C. Miller. 2002. A biological role for prokaryotic CLC chloride channels. *Nature.* 419:715–718. <https://doi.org/10.1038/nature01000>

Iyer, R., C. Williams, and C. Miller. 2003. Arginine-agmatine antiporter in extreme acid resistance in *Escherichia coli*. *J. Bacteriol.* 185:6556–6561. <https://doi.org/10.1128/JB.185.22.6556-6561.2003>

Kowalczyk, L., M. Ratera, A. Paladino, P. Bartoccioni, E. Errasti-Murugarren, E. Valencia, G. Portella, S. Bial, A. Zorzano, I. Fita, et al. 2011. Molecular basis of substrate-induced permeation by an amino acid antiporter. *Proc. Natl. Acad. Sci. USA.* 108:3935–3940. <https://doi.org/10.1073/pnas.1018081108>

Krammer, E.M., and M. Prévost. 2019. Function and regulation of acid resistance antiporters. *J. Membr. Biol.* 252:465–481. <https://doi.org/10.1007/s00232-019-00073-6>

Lewis, J.H., R.M. Jamiolkowski, M.S. Woody, E.M. Ostap, and Y.E. Goldman. 2017. Deconvolution of camera instrument response functions. *Biophys. J.* 112:1214–1220. <https://doi.org/10.1016/j.bpj.2017.02.014>

Lewis, J.H., and Z. Lu. 2019a. Resolution of ångström-scale protein conformational changes by analyzing fluorescence anisotropy. *Nat. Struct. Mol. Biol.* 26:802–807. <https://doi.org/10.1038/s41594-019-0274-2>

Lewis, J.H., and Z. Lu. 2019b. Energetics of ångström-scale conformational changes in an RCK domain of the MthK K⁺ channel. *Nat. Struct. Mol. Biol.* 26:808–815. <https://doi.org/10.1038/s41594-019-0275-1>

Lewis, J.H., and Z. Lu. 2019c. Integrating spatiotemporal features of a ligand-regulated, multi-state allosteric protein. *Nat. Struct. Mol. Biol.* 26: 816–822. <https://doi.org/10.1038/s41594-019-0276-0>

Lippert, L.G., T. Dadash, J.A. Hadden, V. Karnawat, B.T. Diroll, C.B. Murray, E.L.F. Holzbaur, K. Schulten, S.L. Reck-Peterson, and Y.E. Goldman. 2017. Angular measurements of the dynein ring reveal a stepping mechanism dependent on a flexible stalk. *Proc. Natl. Acad. Sci. USA.* 114: E4564–E4573. <https://doi.org/10.1073/pnas.1620149114>

Ohmachi, M., Y. Komori, A.H. Iwane, F. Fujii, T. Jin, and T. Yanagida. 2012. Fluorescence microscopy for simultaneous observation of 3D

orientation and movement and its application to quantum rod-tagged myosin V. *Proc. Natl. Acad. Sci. USA.* 109:5294–5298. <https://doi.org/10.1073/pnas.1118472109>

Post, R.L., C. Hegvany, and S. Kume. 1972. Activation by adenosine triphosphate in the phosphorylation kinetics of sodium and potassium ion transport adenosine triphosphatase. *J. Biol. Chem.* 247:6530–6540. [https://doi.org/10.1016/S0021-9258\(19\)44725-X](https://doi.org/10.1016/S0021-9258(19)44725-X)

Press, W.H., S.A. Teukolsky, W.T. Vetterling, and B.P. Flannery. 2007. *Numerical Recipes: The Art of Scientific Computing*. Cambridge University Press, New York, NY, USA.

Ritchie, T.K., Y.V. Grinkova, T.H. Bayburt, I.G. Denisov, J.K. Zolnerciks, W.M. Atkins, and S.G. Sligar. 2009. Reconstitution of membrane proteins in phospholipid bilayer nanodiscs. *Methods Enzymol.* 464:211–231. [https://doi.org/10.1016/S0076-6879\(09\)64011-8](https://doi.org/10.1016/S0076-6879(09)64011-8)

Rosenberg, S.A., M.E. Quinlan, J.N. Forkey, and Y.E. Goldman. 2005. Rotational motions of macro-molecules by single-molecule fluorescence microscopy. *Acc. Chem. Res.* 38:583–593. <https://doi.org/10.1021/ar040137k>

Sajed, T., A. Marcu, M. Ramirez, A. Pon, A.C. Guo, C. Knox, M. Wilson, J.R. Grant, Y. Djoumbou, and D.S. Wishart. 2016. ECMDB 2.0: A richer resource for understanding the biochemistry of *E. coli*. *Nucleic Acids Res.* 44:D495–D501. <https://doi.org/10.1093/nar/gkv1060>

Sakmann, B., and E. Neher. 1995. *Single-Channel Recording*. Plenum Press, New York, NY, USA.

Sase, I., H. Miyata, S. Ishiwata, and K. Kinosita Jr. 1997. Axial rotation of sliding actin filaments revealed by single-fluorophore imaging. *Proc. Natl. Acad. Sci. USA.* 94:5646–5650. <https://doi.org/10.1073/pnas.94.11.5646>

Shaffer, P.L., A. Goehring, A. Shankaranarayanan, and E. Gouaux. 2009. Structure and mechanism of a Na^+ -independent amino acid transporter. *Science*. 325:1010–1014. <https://doi.org/10.1126/science.1176088>

Shi, Y. 2013. Common folds and transport mechanisms of secondary active transporters. *Annu. Rev. Biophys.* 42:51–72. <https://doi.org/10.1146/annurev-biophys-083012-130429>

Sosa, H., E.J. Peterman, W.E. Moerner, and L.S. Goldstein. 2001. ADP-induced rocking of the kinesin motor domain revealed by single-molecule fluorescence polarization microscopy. *Nat. Struct. Biol.* 8:540–544. <https://doi.org/10.1038/88611>

Tsai, M.F., Y. Fang, and C. Miller. 2012. Sided functions of an arginine-agonatine antiporter oriented in liposomes. *Biochemistry*. 51:1577–1585. <https://doi.org/10.1021/bi201897t>

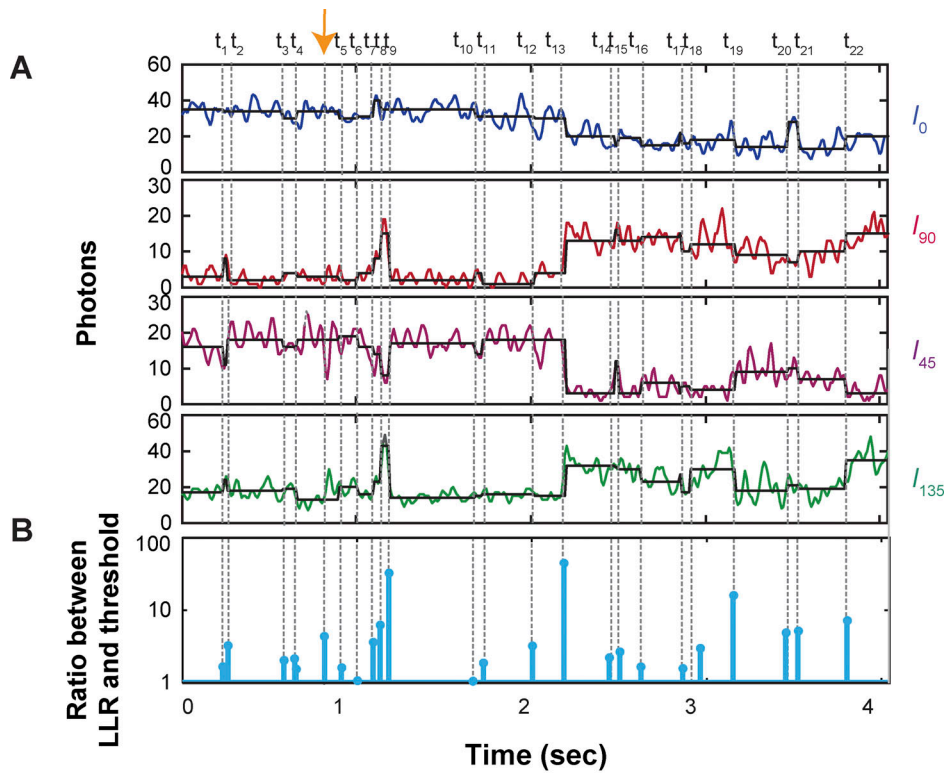
Tsai, M.F., and C. Miller. 2013. Substrate selectivity in arginine-dependent acid resistance in enteric bacteria. *Proc. Natl. Acad. Sci. USA.* 110: 5893–5897. <https://doi.org/10.1073/pnas.1301442110>

Warshaw, D.M., E. Hayes, D. Gaffney, A.M. Lauzon, J. Wu, G. Kennedy, K. Trybus, S. Lowey, and C. Berger. 1998. Myosin conformational states determined by single fluorophore polarization. *Proc. Natl. Acad. Sci. USA.* 95:8034–8039. <https://doi.org/10.1073/pnas.95.14.8034>

Woody, M.S., J.H. Lewis, M.J. Greenberg, Y.E. Goldman, and E.M. Ostap. 2016. MEMLET: An easy-to-use tool for data fitting and model comparison using maximum-likelihood estimation. *Biophys. J.* 111:273–282. <https://doi.org/10.1016/j.bpj.2016.06.019>

Zhou, Y., J.H. Lewis, and Z. Lu. 2023. Tracking multiple conformations occurring on angstrom-and-millisecond scales in single amino-acid-transporter molecules. *Elife*. 12:e82175. <https://doi.org/10.7554/elife.82175>

Supplemental material



$$LLR = \sum_{r=1}^4 m_r \ln \left(\frac{m_r}{\tau} \right) + (N_r - m_r) \ln \left(\frac{N_r - m_r}{T - \tau} \right) - N_r \ln \left(\frac{N_r}{T} \right)$$

Figure S1. Changepoint analysis of a set of polarized intensity components. **(A)** The intensities of four polarized components are replotted from Fig. 1 A. Dashed vertical thin lines indicate individual finally identified intensity transitions, t_1 – t_{22} , and a false positive one between t_4 – t_5 . **(B)** The ratio between LLR and the 95% confidence threshold is plotted for each identified transition. The equation to calculate LLR is given at the bottom (Lewis and Lu, 2019a), in which m_r is the number of photons detected during the duration τ from the beginning of a time segment and the evaluated time point, whereas N_r is the total number of photons detected during the total duration T of the segment. The final LLR is the sum of those for the individual four polarized components of intensity. As expected, all values are above one. By definition, for a 95% confidence detection threshold, 1 false positive occurs for every 20 identified transitions on average. Here, among the total 23 positives, the one pointed at by the orange arrow is judged to be false on the basis that it is a transition within C_1 itself (see Results). Consequently, the number of finally identified intensity transitions is reduced by one to 22. LLR: log maximum likelihood ratio.

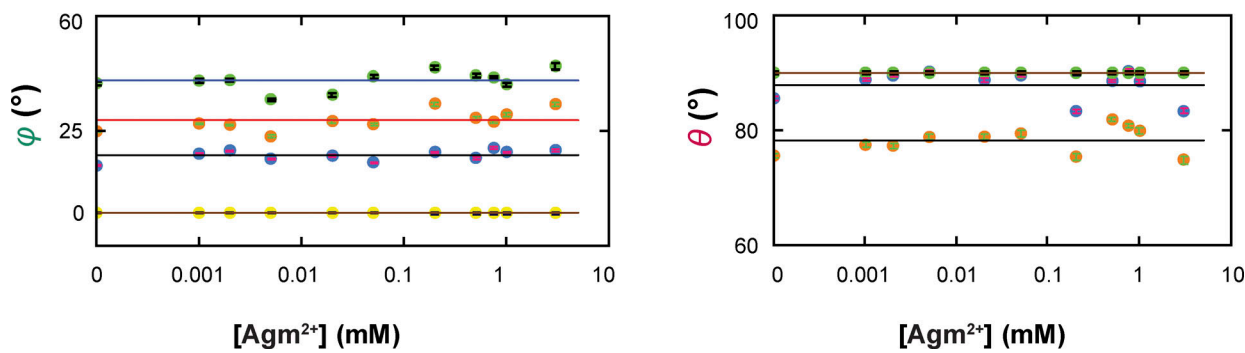


Figure S2. **Average angle values of individual conformational states in a series of Agm^{2+} concentrations.** The values of θ and φ (mean \pm SEM) for each of the four conformations are plotted against the concentration of Agm^{2+} . The number of events is 945–3,187. The symbols for the conformational state C_1 are colored yellow, C_2 colored blue, C_3 colored orange, and C_4 colored cyan. Note that as described in Results, mean θ for either C_1 (yellow) or C_4 (cyan) are set to 90° and are thus overlapped.

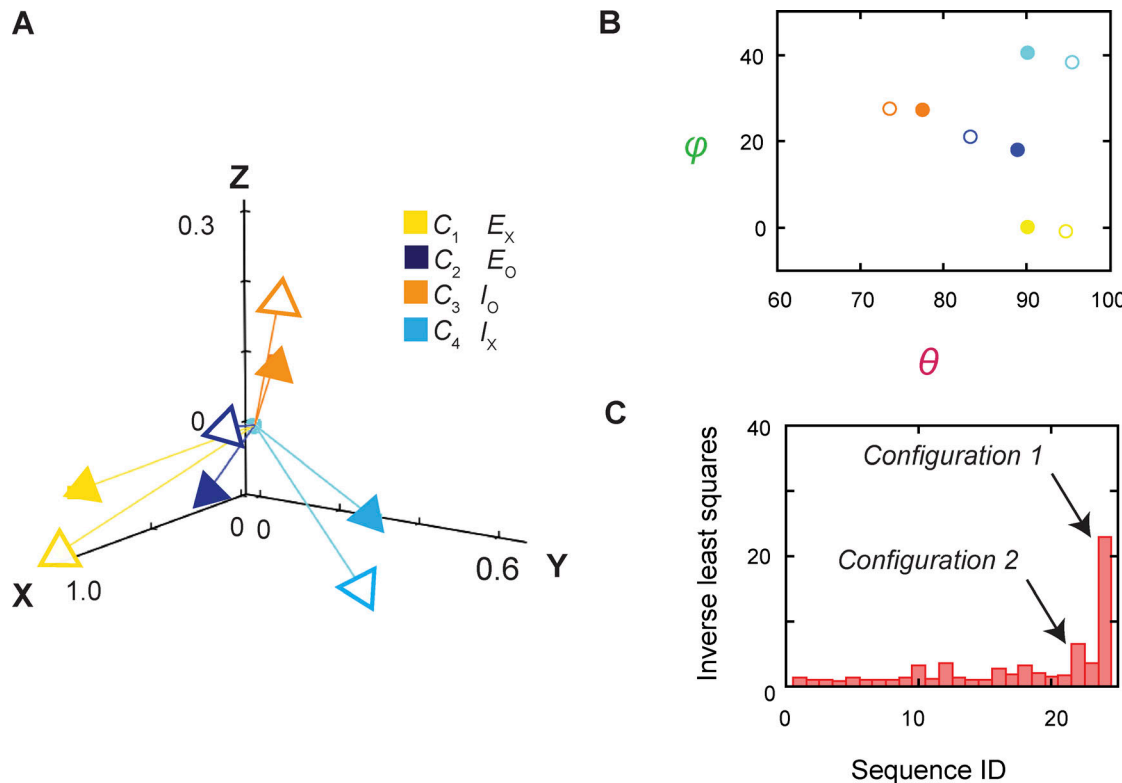


Figure S3. **Relations between the structural and conformational states determined, respectively, from the crystal structures and in the polarization study.** (A) The four mean orientations of the tracked helix in the four conformational states, determined over the examined range of the Agm^{2+} concentration, are represented by a set of four unit vectors (closed heads) in the local coordinates, whereas those for four structural states by another set of unit vectors (open heads), which are E_O (blue) (PDB: 7O82) and E_X (yellow) (PDB: 3L1L) of AdiC, I_O of BasC (orange) (PDB: 6F2G), and I_X of Apct (cyan) (PDB: 3GIA). The vectors for the conformational states, color coded for the states, are drawn according to θ and φ values obtained from the corresponding distributions. The two sets of vectors are overlaid according to the combined least-distance squares. (B) Scatter plots of mean θ versus φ values for four conformational states (closed circles), which are compared with those for the four structural states (open circles); all are color coded for states. (C) The inverse values of combined least-distance squares between the locations of the arrow heads of the two compared groups (open versus closed) in panel A plotted against the identification (ID) numbers for all 24 possible combination sequences among them. The two cases corresponding to configurations 1 and 2 are indicated by the arrows.

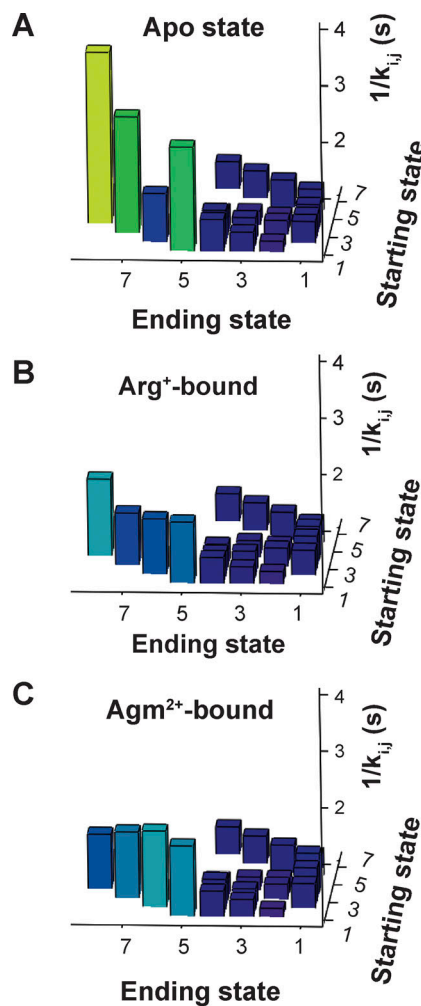
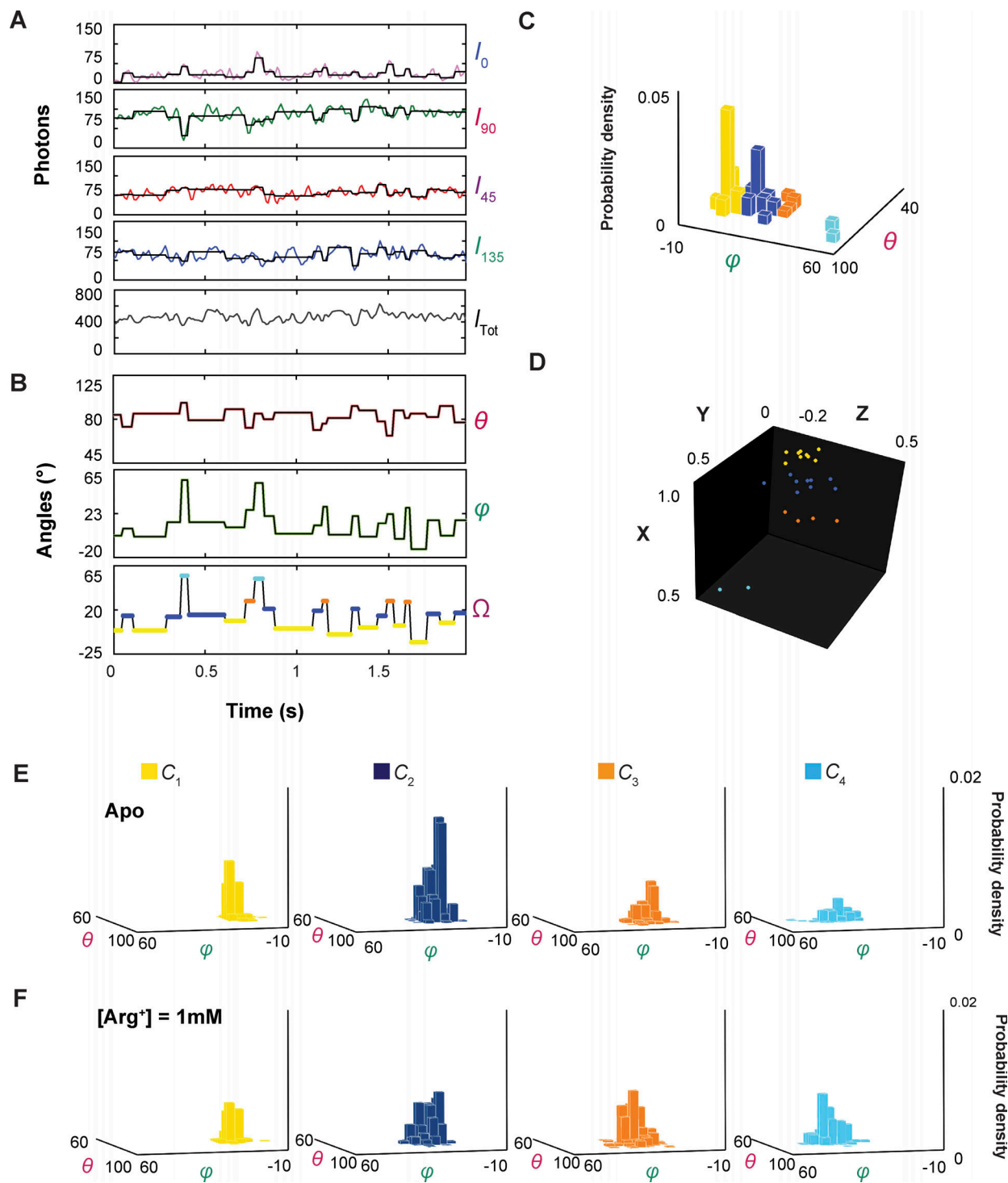


Figure S4. Comparison of state-to-state transition rate constants of AdiC. (A-C) The reciprocals of the rate constants ($1/k_{ij}$) plotted against the starting state i and the ending state j . The four taller columns correspond to the reciprocals of $k_{1,5}$, $k_{2,6}$, $k_{3,7}$, and $k_{4,8}$ in the absence (A) or the presence of Arg⁺ (B) or Agm²⁺ (C). The columns are color coded according to their height, namely, changing from blue toward yellow as the height increases.



Downloaded from http://jupress.org/jgp/article-pdf/157/3/e202413709/1939238/jgp_202413709.pdf by guest on 09 February 2026

Figure S5. The behaviors of a monofunctional fluorophore-attached helix 6A. **(A)** The intensities recorded from a monofunctional fluorophore attached to an AdiC molecule in the absence of any substrate. Individual components are color coded and plotted against the observation time. Each black vertical line in the black traces, superimposed on the colored intensity traces, indicates the time point at which a change in the intensities and thus fluorophore's orientation is identified, whereas each black horizontal line represents the mean intensity between two identified consecutive time points. **(B)** Traces for θ and φ are calculated from the black traces in A and expressed in the local frame of reference defined in Results. Values for the Ω trace are calculated from the θ and φ traces relative to the mean values for C_1 , where the states are color coded. **(C)** The 3D probability densities of individual conformational states plotted against θ and φ values. The θ and φ values for individual events are determined from the particle exhibited in panel A. **(D)** The positions of the arrowheads of individual vectors that represents the orientations of the fluorophore dipole in the individual events of adopting various conformations are mapped onto a unit sphere defined by the Cartesian coordinates of the local framework described in Results. The x, y, and z positions are calculated from θ and φ plotted in panel C, with a radius of a unit length that carry no physical meaning here. **(E and F)** Ensemble 3D probability density distributions of θ and φ in the absence (apo) and the presence of 1 mM Arg^+ . The distributions were built with the data analyzed from 25 to 36 particles with a total of 584–699 events. The histograms (C, E, and F) and data points (D) for conformational state C_1 are colored yellow, C_2 colored blue, C_3 colored orange, and C_4 color cyan.

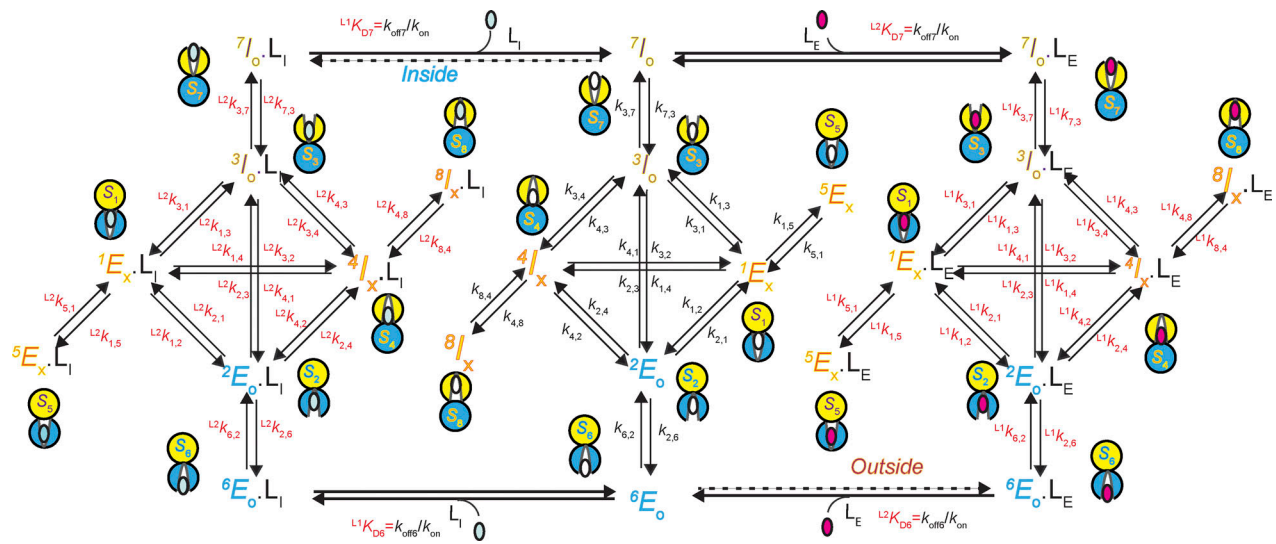


Figure S6. A 24-state kinetic model of AdiC for transporting two types of ligand on opposite sides of the membrane. All states are denoted according to the sidedness configuration 1 described in Results. As an example, S_6 identified in the polarization study, which corresponds to the structural and functional state E_O , is denoted as $6E_O$ (bottom middle). The middle portion described the transition of apo AdiC among eight identified states differing in conformation or energy. The left and right portions describe the transport of the intracellular ligand L_I , e.g., Agm^{2+} or a nonradioactive ligand, and the extracellular ligand L_E , e.g., Arg^+ or a radioactive ligand, respectively. As initial conditions, L_I is only present in the internal solution, whereas L_E is only present in the external solution. After being transported across the membrane, they are present on both sides. Transition rate constants $k_{i,j}$ and $k_{j,i}$ associated with arrows, indicate the reversible transitions between corresponding states i and j (Tables S1, S2, S3, and S4). For distinction, the transitions involving the binding and unbinding of a ligand are labeled with $K_D = k_{off}/k_{on}$.

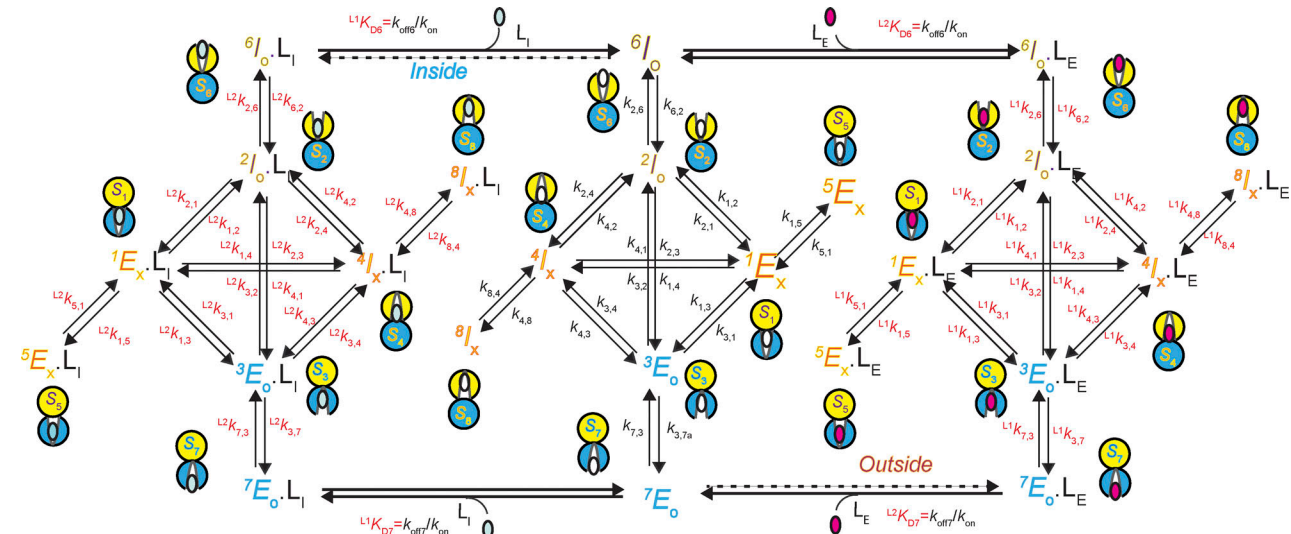


Figure S7. An alternative 24-state kinetic model of AdiC for transporting two types of ligand on opposite sides of the membrane. The model is the same as the one shown in Fig. S6, except that E_O and L_O are switched such that it becomes the sidedness configuration 2.

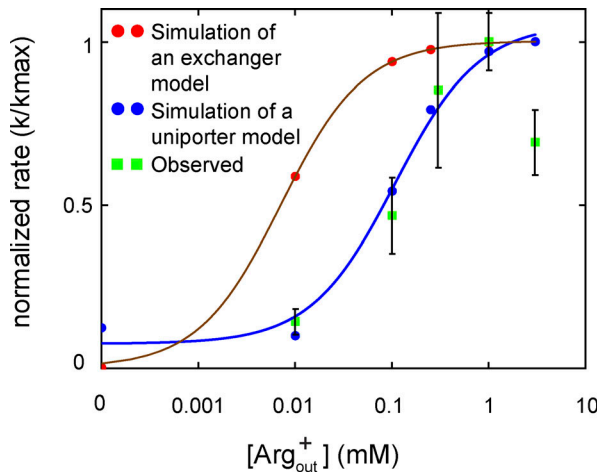


Figure S8. **Simulation of the dependence of the Agm^{2+} -efflux rate from bacteria on the Arg^+ concentration in the medium.** The previously observed initial rate of Agm^{2+} extrusion at pH 2.5 (mean \pm SEM; closed green squares) is normalized relative to the observed maximum and replotted here against the external Arg^+ concentration on a logarithmic scale (Iyer et al., 2003). The simulations using the model (with kinetic parameters determined in the polarization study at the corresponding pH) shown in Fig. S6 itself or with its apo path for conformational transitions eliminated, i.e., a uniporter or an exchanger model, are shown as closed blue or red circles (see supplemental text at the end of the PDF). The red curve is a fit of a Michaelis–Menten equation to the data simulated with the exchanger model, whereas the blue curve is a fit of a modified Michaelis–Menten equation to the data simulated with the uniporter model. The modification allows the rate to approach a nonzero minimum value as the external Arg^+ concentration approaches zero.

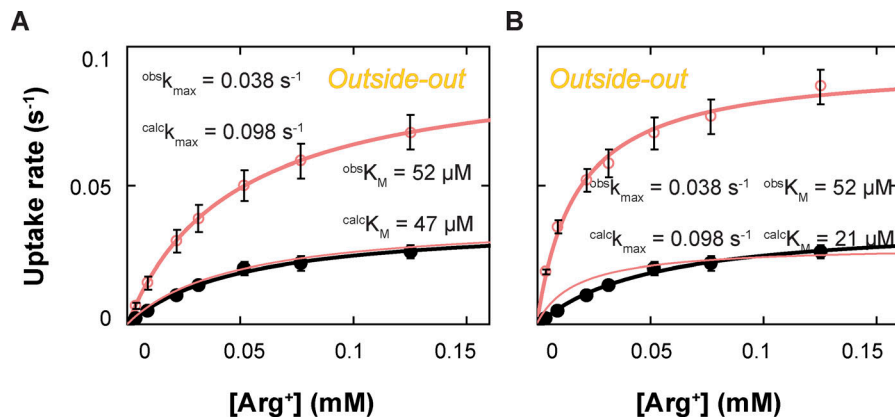


Figure S9. **Comparison of the observed and calculated rates of the AdiC-mediated uptake of Arg^+ into lipid vesicles in the outside-out configuration.** (A and B) Observed uptake rates of Arg^+ (closed black circles; mean \pm SEM) (Tsai et al., 2012) and the predicted rates by the model (open pink circles; mean \pm SD), plotted against the Arg^+ concentration. In panel A, C_2 being assigned as E_o and C_3 as I_o (Fig. S6), whereas in panel B, C_2 as I_o and C_3 as E_o (Fig. S7). The solid curves superimposed on symbols representing the calculated values correspond to the fits of the Michaelis–Menten equation. In the presence of near saturating concentrations of a given type of substrate on both sides of the membrane, the observed maximal net-flux rates (k_{\max}) are expected to be comparable in both orientations of AdiC. Indeed, under the three conditions that differ in substrate type or AdiC orientation, k_{\max} values are comparable (Fig. 12). However, observed k_{\max} for Arg^+ in the outside-out orientation shown here is much lower, which reflects an underestimate of the maximal transporting rate or an overestimate of the effective number of AdiC molecules or both. Our calculations, as expected, yield comparable k_{\max} values for all four conditions. The divergence between observed and calculated k_{\max} values in the outside-out configuration is illustrated graphically by overlaying the observed data and the thin pink curve that represents a Michaelis–Menten equation fit to the calculated data in A or B after scaling down.

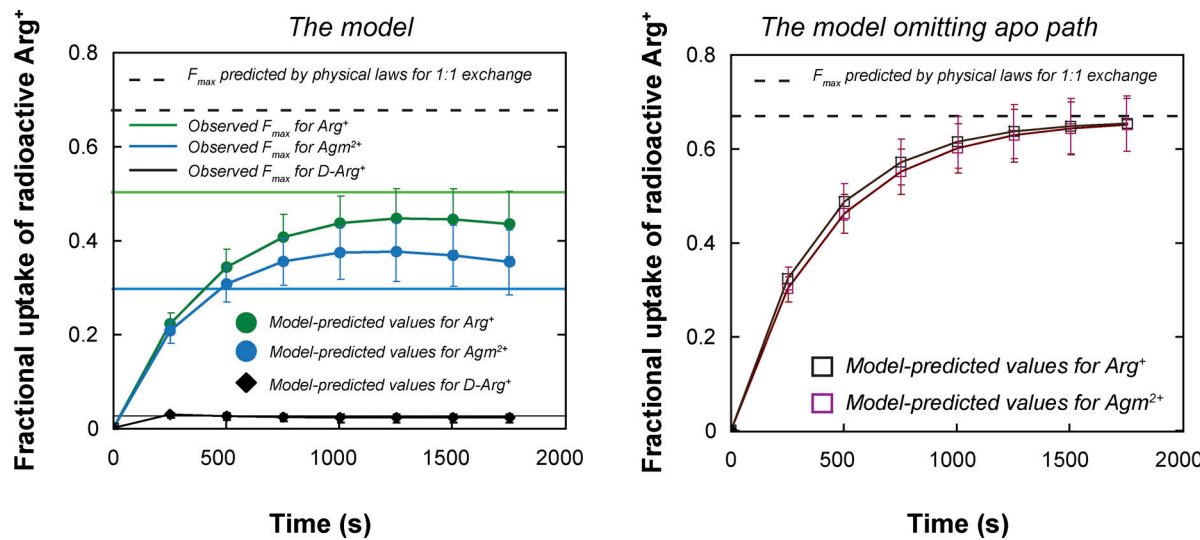


Figure S10. Model-predicted uptakes of radioactive Arg⁺ into AdiC-embedded lipid vesicles compared with the observed and theoretical maximum values. (A) The model-predicted fractions of radioactive Arg⁺ (mean \pm σ) accumulated inside the vesicles for individual indicated durations were obtained from the simulation with the model (Fig. S6), as shown in Fig. 11 A (see Results, and supplemental text at the end of the PDF), under the initial conditions that the bathing solution always contained 50 μ M radioactive Arg⁺, whereas the vesicles contained 5 mM Agm²⁺ (closed blue circles), 5 mM Arg⁺ (closed green circles), or 5 mM functionally inert D-Arg⁺ (closed black circles), compared with the previously F_{max}^{obs} for the corresponding conditions indicated by the solid lines in the respective color (Fang et al., 2007). The dashed line at the top indicates the theoretical F_{max} for an obligatory 1:1 exchange under the initial conditions that the bathing solution always contained 50 μ M radioactive Arg⁺, whereas the vesicles contained 5 mM Agm²⁺ or Arg⁺ (Eq. 10). **(B)** The model-predicted time-dependent fractions of radioactive Arg⁺ uptake (mean \pm σ) were obtained from the simulation with the model after omitting the apo path for confirmational transitions, under the initial condition that the bathing solution always contained 50 μ M radioactive Arg⁺, whereas the vesicles contained 5 mM Arg⁺ (open black squares) or Agm²⁺ (open maroon squares), compared with the theoretical F_{max} indicated by the black dashed line.

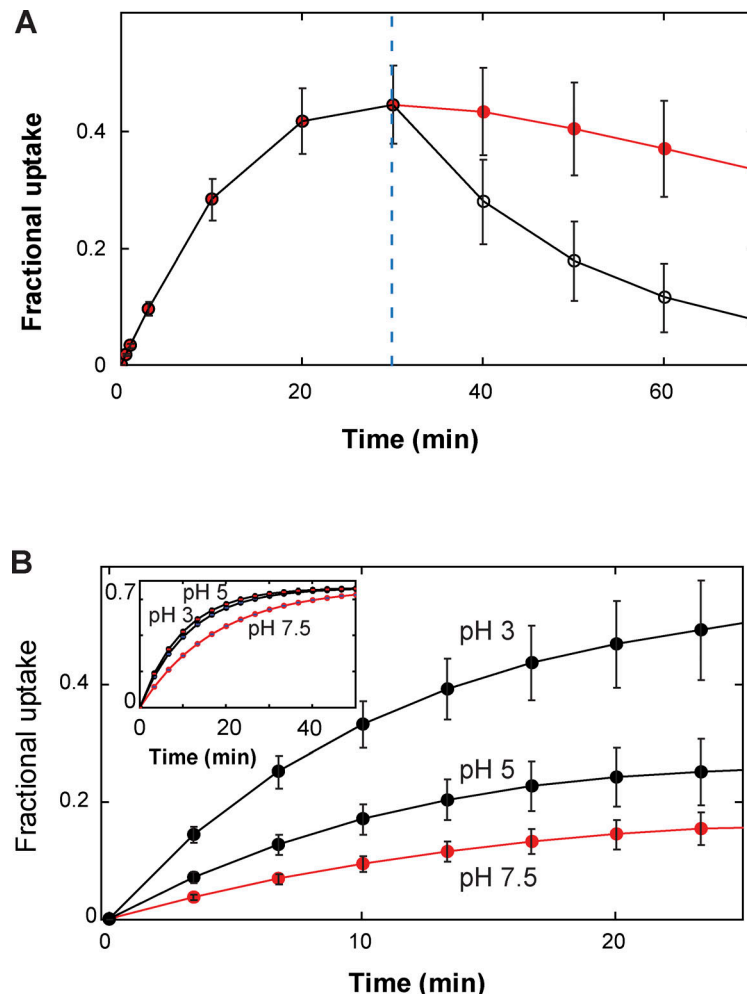


Figure S11. Simulations of radioactive Arg⁺ efflux induced by lowering the Arg⁺ concentration in the bathing solution and the variation of fractional uptake of radioactive Arg⁺ with a symmetric change in pH. (A and B) The time courses of fractional uptake of radioactive Arg⁺ (mean \pm σ) were simulated using our model with the parameters determined from the polarization measurements under the symmetric pH conditions. As the initial substrate conditions, the vesicles contained 5 mM Arg⁺, whereas the bathing solution contained 50 μ M radioactive Arg⁺. The ratio of volumes of the bathing solution and vesicles was 50. **(A)** 30 min into the simulation, the calculation was continued either without any intervention (closed red circles) or with the Arg⁺ concentration of the bathing solution being raised to 5 mM (open black circles), the latter of which markedly lowered the fractional uptake in a time-dependent manner or induced an efflux of radioactive Arg⁺. **(B)** The simulations were performed with our model (of kinetic parameters determined in the polarization study at the corresponding pH) under three conditions where pH was varied symmetrically on both sides of the membrane. For comparison, the simulations under the same conditions with the model whose apo path for conformational transitions was eliminated were shown in the inset. Note that Tsai et al. (2012) showed that mutant AdiC with native cysteines removed had slower kinetics than wild-type AdiC. As expected, the kinetics of the simulated time courses using our model with the kinetic parameters obtained from an AdiC mutant with native cysteines removed are slower than those of wild-type AdiC reported by Fang et al. (2007) but are comparable with those of the mutant AdiC reported by Tsai et al. (2012).

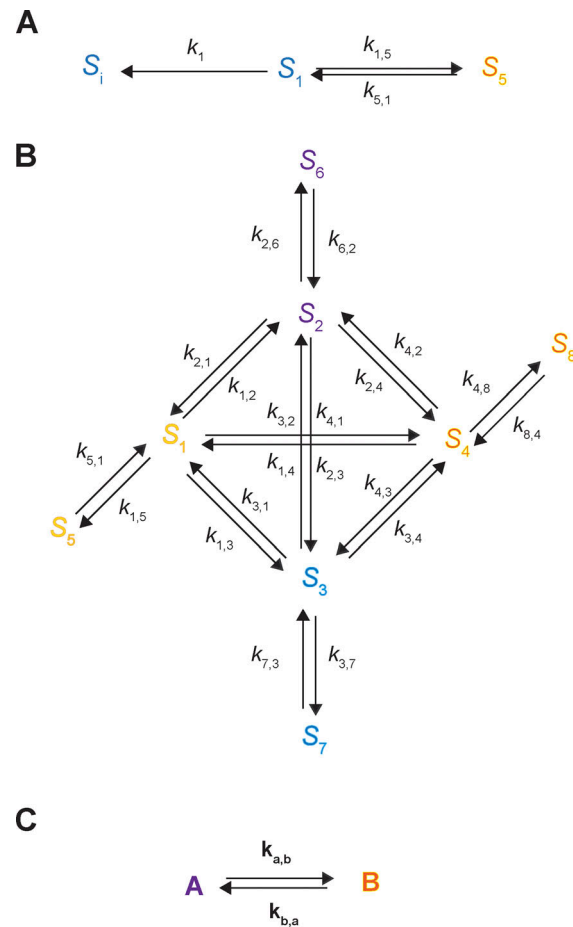


Figure S12. **Portions of the 24-state kinetic model.** (A) Diagram of the states S_1 and S_5 with the corresponding forward and backward rates $k_{1,5}$ and $k_{5,1}$, which are the energetic states underlying the conformation state C_1 . S_1 also transitions to an ensemble of S_2 , S_3 , or S_4 , denoted as S_i with an apparent ensemble rate constant k_i , as described in the supplemental text at the end of the PDF. (B) Diagram of the eight apo states S_1 – S_8 , which corresponds to the middle section in Fig. 6. The transition matrix Q_{apo} corresponding to this diagram is given in Eq. S25. (C) The eight-state model in the panel B is reduced to a system with two ensemble-state components, A and B, where A comprises the states S_1 – S_4 , whereas B comprises the states S_5 – S_8 . The corresponding transition matrix is given in Eq. S26.

Video 1. **A composite video exhibiting intensities of polarized emission of a fluorophore attached to an AdiC protein molecule shown in Fig. 1, integrated intensity values, calculated angles, and electron densities of AdiC in different conformations.** Shown on the left are the original recorded intensities I_0 , I_{45} , I_{90} , and I_{135} displayed from top to bottom; on the middle left are running traces of integrated intensity values with background subtracted; on the middle right are running traces of angles θ and φ along with Ω , where each event is color coded according to the state that AdiC adopts; C_1 (yellow) corresponds to the E_x conformation, C_2 (blue) to E_0 , C_3 (orange) to I_0 , and C_4 (cyan) to I_x ; on the right is a video of the AdiC molecule transitioning among four conformational states represented by the electron densities of AdiC (PDBs 7082 and 3L1L) and those of the related BasC and ApcT transporters proper (PDBs 6F2G and 3GIA), as described in Results. At a given time point, the electron density corresponding to the conformation identified by the polarization study is displayed. Due to the limit of allowable file size, the video was made to be viewed in a small window of such software as Windows Media Player.

Video 2. **Video of simulation of a counter transport of Arg^+ and Agn^{2+} by AdiC.** As described in Results, at a given time point, the crystal structure model for a specific state is displayed according to the template shown in Fig. 11 A. The C_1 (yellow) state corresponds to the E_x conformation, C_2 (light blue) to E_0 , C_3 (orange) to I_0 , and C_4 (cyan) to I_x . The structures in E_0 and E_x are those of AdiC (PDBs 7082 and 3L1L), whereas I_0 and I_x are those of the related BasC and ApcT transporters proper (PDBs 6F2G and 3GIA). Arg^+ (shown in green) is transported from the external (top) side to the intracellular (bottom) side, whereas Agn^{2+} (shown in maroon) is transported in the opposite direction. Throughout the video, external Arg^+ and internal Agn^{2+} are both kept at constant 1 mM. The number of transported substrate molecules is assumed to be negligible with respect to the total number of available substrate molecules. Due to the limit of allowable file size, the video was made to be viewed in a small window of such software as Windows Media Player.

Provided online are 13 tables. Table S1 shows the analysis results of lifetimes and transition probabilities for state $C1$ of AdiC in the absence or presence of Arg^+ or Agn^{2+} . Table S2 shows the analysis results of lifetimes and transition probabilities for state $C2$ of AdiC in the absence or presence of Arg^+ or Agn^{2+} . Table S3 shows the analysis results of lifetimes and transition probabilities for

state C3 of AdiC in the absence or presence of Arg⁺ or Agm²⁺. Table S4 shows the analysis results of lifetimes and transition probabilities for state C4 of AdiC in the absence or presence of Arg⁺ or Agm²⁺. Table S5 shows the probabilities of the four conformational states of AdiC determined with bifunctional or monofunctional probes. Table S6 shows the analysis results of lifetimes and transition probabilities for state C1 of monofunctional ATTO-550 labeled AdiC in the absence or presence of Arg⁺. Table S7 shows the analysis results of lifetimes and transition probabilities for state C2 of monofunctional ATTO-550 labeled AdiC in the absence or presence of Arg⁺. Table S8 shows the analysis results of lifetimes and transition probabilities for state C3 of monofunctional ATTO-550 labeled AdiC in the absence or presence of Arg⁺. Table S9 shows the analysis results of lifetimes and transition probabilities for state C4 of monofunctional ATTO-550 labeled AdiC in the absence or presence of Arg⁺. Table S10 shows the probabilities of states in the absence or presence Arg⁺ or Agm²⁺. Table S11 shows the equilibrium dissociation constants of Arg⁺- or Agm²⁺-bound states. Table S12 shows the equilibrium constants in the absence or presence of Arg⁺ or Agm²⁺. Table S13 shows the observed and calculated k_{max} and K_m of Arg⁺ and Agm²⁺.

Determination of rate constants from the parameters yielded from fitting a two-exponential function to the dwell-time distributions
 As the intensity signals were recorded on a camera in discrete units of time Δt , the dwell-time distribution for each of the four conformational states C_1-C_4 was fitted with the following double exponential probability mass function (Lewis et al., 2017):

$$p_{d2}(\tau_1, \tau_2, f) = \frac{f \tau_1 (1 - e^{-\frac{\Delta t}{\tau_1}})^2 e^{-\frac{(t-\Delta t)}{\tau_1}} + (1 - f) \tau_2 (1 - e^{-\frac{\Delta t}{\tau_2}})^2 e^{-\frac{(t-\Delta t)}{\tau_2}}}{f \tau_1 (1 - e^{-\frac{\Delta t}{\tau_1}}) e^{-\frac{(t_m-\Delta t)}{\tau_1}} + (1 - f) \tau_2 (1 - e^{-\frac{\Delta t}{\tau_2}}) e^{-\frac{(t_m-\Delta t)}{\tau_2}}} \quad (S1)$$

in which the missing events that are shorter than t_m are taken into consideration. Statistically, the distributions were much better fitted with such a normalized double-exponential function than a single-exponential function defined as

$$p_d(\tau) = \left(1 - e^{-\frac{\Delta t}{\tau}}\right) e^{-(f-f_m)\frac{\Delta t}{\tau}} \quad (S2)$$

This judgment was made based on all P values being $<10^{-15}$ in F-tests limited by the precision of computer calculation using double-precision floating point numbers (Woody et al., 2016).

Using the apo energetic states S_1 and S_5 as examples, we derived the relations between the three fitted parameters and the three apparent underlying rate constants for a given ligand condition. The part of the 24-state model in Fig. 6, immediately relevant here, is summarized in Fig. S12 A. In this part, S_1 and S_5 are reversibly connected with the rate constants k_{15} and k_{51} ; S_1 can also transition to S_2 , S_3 , or S_4 (together denoted as S_i) via three parallel pathways, represented by a single step to S_i , with the combined rate constant k_1 , whereas the reversed three paths whose combined rate constants would be denoted by k_{-1} are not contributing factors of the lifetime distribution of C_1 that is split to S_1 and S_5 .

The system of rate equations for the part of the model represented in Fig. S12 A is expressed as

$$\frac{d\mathbf{p}'(t)}{dt} = \mathbf{k}' \mathbf{p}'(t) \quad (S3)$$

with \mathbf{p}' and \mathbf{k}' defined as

$$\mathbf{p}'(t) = \begin{bmatrix} p'_1(t) \\ p'_5(t) \end{bmatrix} \quad (S4)$$

$$\mathbf{k}' = \begin{bmatrix} -(k_1 + k_{15}) & k_{51} \\ k_{15} & -k_{51} \end{bmatrix} \quad (S5)$$

Eq. S3 represents a homogeneous linear system of ordinary differential equations. The general solution for this kind of system is a set of two-exponential functions expressed as

$$\begin{bmatrix} p'_1(t) \\ p'_5(t) \end{bmatrix} = \begin{pmatrix} A_1 e^{-\lambda_1 t} + B_1 e^{-\lambda_2 t} \\ A_2 e^{-\lambda_1 t} + B_2 e^{-\lambda_2 t} \end{pmatrix} \quad (S6)$$

where the apparent rates λ_1 and λ_2 are convolutions of the rates k_1 , k_{15} , and k_{51} . The relationship between them can be obtained from the eigenvalues of \mathbf{k}' by evaluating the following determinant set to zero:

$$|\mathbf{k}' - \lambda \mathbf{I}| = \lambda^2 - (k_1 + k_{15} + k_{51})\lambda + k_1 k_{51} = 0 \quad (S7)$$

where the two roots of λ are

$$\begin{aligned}\lambda_1 &= \frac{1}{2} \left[(k_1 + k_{15} + k_{51}) + \sqrt{(k_1 + k_{15} + k_{51})^2 - 4k_{51}k_1} \right] \\ \lambda_2 &= \frac{1}{2} \left[(k_1 + k_{15} + k_{51}) - \sqrt{(k_1 + k_{15} + k_{51})^2 - 4k_{51}k_1} \right]\end{aligned}\quad (\text{S8})$$

The probabilities of observing S_1 and S_5 are given by Eq. S6, based on the assumption that they can be distinguished from one another. However, in the present case, S_1 and S_5 are observed indistinguishably in terms of spatial orientation as the conformational state C_1 (see Results). The expression for C_1 is then given by

$$C_1(t) = p'_1(t) + p'_5(t) = (A_1 + A_2)e^{-\lambda_1 t} + (B_1 + B_2)e^{-\lambda_2 t} \quad (\text{S9})$$

where λ_1 and λ_2 are defined by Eq. S8. Normalized to a probability distribution function, Eq. S9 becomes

$$P_1(t) = fe^{-\lambda_1 t} + (1-f)e^{-\lambda_2 t} \quad (\text{S10})$$

Operationally, the relative amplitude of the first (fast) component, f , can be conveniently found from its relation to the observed average lifetime τ_{av} of C_1 (i.e., " $S_1 + S_5$ "):

$$\tau_{\text{av}} = f \frac{1}{\lambda_1} + (1-f) \frac{1}{\lambda_2} \quad (\text{S11})$$

The average lifetime for the kinetic process shown in Fig. S12 A can in turn be calculated from the rate constants through the following expression (Sakmann and Neher, 1995):

$$\tau_{\text{av}} = \left(\frac{k_{15}}{k_{15} + k_{51}} \right) \bullet \left[-\mathbf{k}^{-1} \bullet \begin{pmatrix} 1 \\ 1 \end{pmatrix} \right] = \frac{k_{51}k_1}{k_{15} + k_{51}} \quad (\text{S12})$$

from which the following expression for f can be obtained:

$$f = \frac{\tau_{\text{av}} - \frac{1}{\lambda_2}}{\frac{1}{\lambda_1} - \frac{1}{\lambda_2}} = \frac{\frac{k_{51}k_1}{k_{15} + k_{51}} - \frac{1}{\lambda_2}}{\frac{1}{\lambda_1} - \frac{1}{\lambda_2}} \quad (\text{S13})$$

Then, the rate constants k_1 , k_{15} , and k_{51} can be calculated from λ_1 , λ_2 , and f as

$$k_{15} = \frac{f(1-f)(\lambda_1 - \lambda_2)^2}{f\lambda_1 + (1-f)\lambda_2} \quad (\text{S14})$$

$$k_{51} = \frac{\lambda_1\lambda_2}{f\lambda_1 + (1-f)\lambda_2} \quad (\text{S15})$$

$$k_1 = f\lambda_1 + (1-f)\lambda_2 \quad (\text{S16})$$

in which λ_1 , λ_2 , and f can in turn be obtained from a fit of the double exponential probability mass function to the dwell-time distribution of C_1 ($S_1 + S_5$), as described above.

Furthermore, the three rate constants that sum to k_1 can be determined as described below. The total effective rate k_1 of exiting S_1 via the three parallel transitions would be the sum of the rate constants $k_{1,2}$, $k_{1,3}$, and $k_{1,4}$. Generally, the rate (k_i) of exiting state S_i to one of m possible states should be expressed as

$$k_i = \sum_{j=1}^m k_{i,j} \quad (\text{S17})$$

where $k_{i,j}$ is given by

$$k_{i,j} = p_{i,j}k_i \quad (\text{S18})$$

Thus, individual $k_{i,j}$ could be determined from the calculated rate k_i , once all relevant $p_{i,j}$ values were determined. We calculated these $p_{i,j}$ values from the ratio of the observed number of C_i -to- C_j transitions ($n_{i,j}$) and the total number of C_i events (N_i):

$$p_{i,j} = \frac{n_{i,j}}{N_i} \quad (\text{S19})$$

where $N_i = \sum_{j=1}^m n_{i,j}$.

Kinetic mechanism for AdiC transporter

To evaluate the substrate flux in the framework of the full model that contains eight states for apo, L_1 -bound or L_2 -bound, totaling 24 states (Fig. 6), the concurrent steady-state substrate-net-flux rates for L_1 and L_2 are separately calculated for a given set of conditions. The flux is defined as the difference between actual forward and backward rates, not rate constants. Thus, in the kinetic model (Fig. 6), the net flux rate of substrates of a given ligand, e.g., L_1 , on both sides of the membrane for a transition, e.g., between S_2 and S_6 with L_1 bound, can be expressed as

$$Flux = {}^{L_1}Flux_{2,6} = {}^{L_1}k_{2,6} {}^{L_1}p_2 - {}^{L_1}k_{6,2} {}^{L_1}p_6 \quad (S20)$$

The first-order rate constants ${}^{L_1}k_{2,6}$ and ${}^{L_1}k_{6,2}$ can be determined as described in Results. As usual, the difficulty of determining the probability of ${}^{L_1}p_2$ or ${}^{L_1}p_6$ at a specified steady-state condition is underscored by the fact that each of them is generally defined by the solution of a differential rate equation, a solution containing all rate constants that specify the relations among all states in the model. The calculation of these probabilities is described below.

At any given time, AdiC may exist in any one of 24 states: 8 apo, 8 L_1 -bound, and 8 L_2 -bound states (Fig. 6). The probabilities of these states are represented by the column vectors ${}^{apo}\mathbf{p}(t)$, ${}^{L_1}\mathbf{p}(t)$, and ${}^{L_2}\mathbf{p}(t)$:

$${}^{apo}\mathbf{p}(t) = \begin{bmatrix} p_1(t) \\ \vdots \\ p_8(t) \end{bmatrix}; {}^{L_1}\mathbf{p}(t) = \begin{bmatrix} {}^{L_1}p_1(t) \\ \vdots \\ {}^{L_1}p_8(t) \end{bmatrix}; {}^{L_2}\mathbf{p}(t) = \begin{bmatrix} {}^{L_2}p_1(t) \\ \vdots \\ {}^{L_2}p_8(t) \end{bmatrix} \quad (S21)$$

When in a system with all three types of states, the probabilities are expressed by the combined vector $\mathbf{p}(t)$:

$$\mathbf{p}(t) = \begin{bmatrix} {}^{apo}\mathbf{p}(t) \\ {}^{L_1}\mathbf{p}(t) \\ {}^{L_2}\mathbf{p}(t) \end{bmatrix} \quad (S22)$$

Determination of the probabilities of the 24 states will be considered in steps, with the 8 apo states alone first. In the 8-state model shown within Fig. S12 B, each observed conformational state (e.g., C_1) has two kinetically connected energetic states (e.g., S_1 and S_5). The transition matrix for the cycle among $S_1 - S_4$ is defined as \mathbf{k} :

$$\mathbf{k} = \begin{pmatrix} -k_1 & k_{21} & k_{31} & k_{41} \\ k_{12} & -k_2 & k_{32} & k_{42} \\ k_{13} & k_{23} & -k_3 & k_{43} \\ k_{14} & k_{24} & k_{34} & -k_4 \end{pmatrix} \quad (S23)$$

where k_i ($i = 1 \dots 4$) is as defined in Results, e.g., $k_1 = k_{12} + k_{13} + k_{14}$, and calculated in accordance with the definition given in Eq. S17, whereas the rate constants $k_{i,j}$ are calculated from k_i and $p_{i,j}$ using Eq. S18, in which $p_{i,j}$ is calculated using Eq. S19. States 5–8 only have one connection each to the main cycle, i.e., S_1 to S_5 , S_2 to S_6 , S_3 to S_7 , and S_4 to S_8 (Fig. S12 B), described by one of four additional forward rate constants $k_{i,i+4}$ and one of four reverse rates $k_{i+4,i}$ that are calculated in accordance with Eqs. S14 and S15. These rate constants can be represented in the diagonal matrices \mathbf{k}_{ab} and \mathbf{k}_{ba} :

$$\mathbf{k}_{ab} = \begin{pmatrix} k_{15} & 0 & 0 & 0 \\ 0 & k_{26} & 0 & 0 \\ 0 & 0 & k_{37} & 0 \\ 0 & 0 & 0 & k_{48} \end{pmatrix}; \mathbf{k}_{ba} = \begin{pmatrix} k_{51} & 0 & 0 & 0 \\ 0 & k_{62} & 0 & 0 \\ 0 & 0 & k_{73} & 0 \\ 0 & 0 & 0 & k_{84} \end{pmatrix} \quad (S24)$$

The 8×8 transition matrix ${}^{apo}\mathbf{Q}$ for the apo state is made up of the rates $k_{i,j}$, $k_{i,i+4}$, and $k_{i+4,i}$:

$${}^{apo}\mathbf{Q} = \begin{pmatrix} -k_1 - k_{15} & k_{21} & k_{31} & k_{41} & k_{51} & 0 & 0 & 0 \\ k_{12} & -k_2 - k_{26} & k_{32} & k_{42} & 0 & k_{62} & 0 & 0 \\ k_{13} & k_{23} & -k_3 - k_{37} & k_{43} & 0 & 0 & k_{73} & 0 \\ k_{14} & k_{24} & k_{34} & -k_4 - k_{48} & 0 & 0 & 0 & k_{84} \\ k_{15} & 0 & 0 & 0 & -k_{51} & 0 & 0 & 0 \\ 0 & k_{26} & 0 & 0 & 0 & -k_{62} & 0 & 0 \\ 0 & 0 & k_{37} & 0 & 0 & 0 & -k_{73} & 0 \\ 0 & 0 & 0 & k_{48} & 0 & 0 & 0 & -k_{84} \end{pmatrix} \quad (S25)$$

For a more concise expression, this eight-state system can alternatively be represented by a system with two ensemble-state components A ($S_1 - S_4$) and B ($S_5 - S_8$) (Fig. S12 C); the rates in B ($S_5 - S_8$) are described by those in matrices \mathbf{k}_{ab} and \mathbf{k}_{ba} (Eq. S24). Using these two matrices and \mathbf{k} from Eq. S23, ${}^{apo}\mathbf{Q}$ can be re-expressed as

$${}_{apo}\mathbf{Q} = \begin{pmatrix} \mathbf{k} - \mathbf{k}_{ab} & \mathbf{k}_{ba} \\ \mathbf{k}_{ab} & -\mathbf{k}_{ba} \end{pmatrix} \quad (S26)$$

For a 16-state model, including 8 apo states and 8 corresponding ligand-bound states, the transition matrices ${}^{L_1}\mathbf{k}$, ${}^{L_1}\mathbf{k}_{ab}$, and ${}^{L_1}\mathbf{k}_{ba}$ would be the same forms as those used for the apo condition in Eqs. S25 and S26, with the rates replaced by ${}^{L_1}k_i$, ${}^{L_1}k_{i,j}$, ${}^{L_1}k_{i,i+4}$, and ${}^{L_1}k_{i+4,i}$ (Fig. 6). Entry of a substrate molecule occurs only at S_6 or S_7 , and exit occurs at ${}^{L_1}S_6$ or ${}^{L_1}S_7$, whereas S_5 , S_8 , ${}^{L_1}S_5$, and ${}^{L_1}S_8$ are occluded cul-de-sac states inaccessible to solution. With these three matrices, the transition matrix for the 16-state model can be given as

$$\mathbf{Q}(L) = \begin{bmatrix} \mathbf{k} - \mathbf{k}_{ab} & \mathbf{k}_{ba} & 0 & 0 \\ \mathbf{k}_{ab} & -(\mathbf{k}_{ba} + {}^{L_1}\mathbf{k}_{on}) & -({}^{L_1}\mathbf{k}_{off}) & 0 \\ 0 & {}^{L_1}\mathbf{k}_{on} & {}^{L_1}\mathbf{k}_{ba} & {}^{L_1}\mathbf{k}_{ab} \\ 0 & 0 & {}^{L_1}\mathbf{k}_{ba} & \mathbf{k} - {}^{L_1}\mathbf{k}_{ab} \end{bmatrix} \quad (S27)$$

where 0 is a 4×4 matrix with zero as each element, and ${}^{L_1}\mathbf{k}_{on}$ and ${}^{L_1}\mathbf{k}_{off}$ are diagonal rate matrices defined as

$${}^{L_1}\mathbf{k}_{on}(L_1) = \begin{pmatrix} 0 & 0 & 0 & 0 \\ 0 & L_{1,in}k_{on6} & 0 & 0 \\ 0 & 0 & L_{1,out}k_{on7} & 0 \\ 0 & 0 & 0 & 0 \end{pmatrix}; \quad {}^{L_1}\mathbf{k}_{off} = \begin{pmatrix} 0 & 0 & 0 & 0 \\ 0 & {}^{L_1}K_{D6}k_{on6} & 0 & 0 \\ 0 & 0 & {}^{L_1}K_{D7}k_{on7} & 0 \\ 0 & 0 & 0 & 0 \end{pmatrix} \quad (S28)$$

For the full 24-state model (Fig. 6) with 8 apo states, 8 L_1 -bound states, and 8 L_2 -bound states, the transition matrix can be formulaically expanded to

$$\mathbf{Q}(L_1, L_2) = \begin{bmatrix} \mathbf{k} - \mathbf{k}_{ab} & \mathbf{k}_{ba} & 0 & 0 & 0 & 0 \\ \mathbf{k}_{ab} & -(\mathbf{k}_{ba} + {}^{L_1}\mathbf{k}_{on}(L_1) + {}^{L_2}\mathbf{k}_{on}(L_2)) & -({}^{L_1}\mathbf{k}_{off}) & 0 & 0 & 0 \\ 0 & {}^{L_1}\mathbf{k}_{on}(L_1) & -({}^{L_1}\mathbf{k}_{ba} + {}^{L_1}\mathbf{k}_{off}) & 0 & 0 & 0 \\ 0 & 0 & {}^{L_1}\mathbf{k}_{ba} & {}^{L_1}\mathbf{k}_{ab} & 0 & 0 \\ 0 & {}^{L_2}\mathbf{k}_{on}(L_2) & 0 & 0 & -({}^{L_2}\mathbf{k}_{ba} + {}^{L_2}\mathbf{k}_{off}) & {}^{L_2}\mathbf{k}_{ab} \\ 0 & 0 & 0 & 0 & {}^{L_2}\mathbf{k}_{ba} & {}^{L_2}\mathbf{k} - {}^{L_2}\mathbf{k}_{ab} \end{bmatrix} \quad (S29)$$

With this transition rate matrix for the 24-state model, we can simultaneously solve the linear system of 24 rate equations:

$$\frac{d\mathbf{p}(t)}{dt} = \mathbf{Q} \cdot \mathbf{p}(t) \quad (S30)$$

For a given steady-state condition, individual state probabilities can be calculated using

$$\mathbf{p}(\infty) = (\mathbf{Q}_a \mathbf{Q}_a^T)^{-1} \mathbf{u} \quad (S31)$$

derived as described below. Mathematically, the system reaches the steady state as $t \rightarrow \infty$, where the derivative becomes zero such that $\mathbf{Q} \cdot \mathbf{p}(\infty) = 0$, with 0 as a zero vector. A solution to the system can be achieved by transforming the argument to the equivalent expression $\mathbf{p}(\infty) \mathbf{Q}_a \mathbf{Q}_a^T = \mathbf{u}$, where \mathbf{u} is a unit vector, \mathbf{Q}_a is \mathbf{Q} augmented by \mathbf{u} (which would be set as an additional rightmost column in \mathbf{Q}_a), and \mathbf{Q}_a^T is transposed \mathbf{Q}_a . Solving $\mathbf{p}(\infty)$ can then be done by multiplying \mathbf{u} by the inverted matrix $(\mathbf{Q}_a \mathbf{Q}_a^T)^{-1}$ (Sakmann and Neher, 1995), which yields above Eq. S31. Following the determination of $\mathbf{p}(\infty)$ that defines the probabilities for all states, including ${}^{L_1}\mathbf{p}_2$ and ${}^{L_1}\mathbf{p}_6$, the expression for the flux ${}^{L_1}Flux_{2,6}$ (Eq. S32) can be calculated, given that the relevant rate constants have already been determined as described above.

Solution of time-dependent state probabilities

The general time-dependent solution for the expression in Eq. S30 is

$$\mathbf{p}(t) = \mathbf{p}(0)e^{-\mathbf{Q} \cdot t} \quad (S32)$$

where the exponential matrix $e^{-\mathbf{Q} \cdot t}$ can be evaluated through an expansion in accordance with the spectral theory in the form of

$$\mathbf{p}(t) = \mathbf{p}(\infty) + \mathbf{p}(0) \sum_{i=2}^{N_{states}} \mathbf{A}_i e^{-\lambda_i \cdot t} \quad (S33)$$

(Sakmann and Neher, 1995). Here, $\mathbf{p}(\infty)$ is from Eq. S31, λ_i are the eigenvalues of matrix \mathbf{Q} (Eq. S29), determined similarly as shown in Eq. S8, and coefficient matrix \mathbf{A}_i is calculated using the eigenvectors \mathbf{X}_i of matrix \mathbf{Q} :

$$\mathbf{A}_i = \mathbf{X}^i \cdot \mathbf{X}_i^{-1} \quad (\text{S34})$$

where \mathbf{X}^i is the column vector of eigenvector matrix \mathbf{X} , and \mathbf{X}_i^{-1} is the row vector of its inverse.

Calculation of the net substrate transport rate for a single subunit of AdiC

For all hereafter described calculations using the kinetic model (Fig. 6), the two alternative configurations of different sidedness (Figs. S6 and S7) were evaluated separately (Figs. 12, 13, and S9).

We calculated the net substrate flux rate across one of the five relevant transitions in the model, including that between S_7 and $S_7.L$, $S_7.L$ and $S_3.L$, $S_3.L$ and $S_2.L$, $S_2.L$ and $S_6.L$, or $S_6.L$ and S_6 (Fig. 6). Each rate is calculated as the difference between the forward and backward rates of the transition, illustrated with the transition between $S_2.L_1$ and $S_6.L_1$, by generating a time- and ligand-dependent flux rate:

$${}^{L_1}\text{Flux}_{2,6}(t) = {}^{L_1}k_{2,6}{}^{L_1}p_2(t) - {}^{L_1}k_{6,2}{}^{L_1}p_6(t) \quad (\text{S35})$$

except for the rate for the S_3L and S_2L transition, which is calculated as

$${}^{L_1}\text{Flux}_{2,3}(t) = [{}^{L_1}k_{2,1}{}^{L_1}p_2(t) - {}^{L_1}k_{1,2}{}^{L_1}p_1(t)] + [{}^{L_1}k_{2,3}{}^{L_1}p_2(t) - {}^{L_1}k_{3,2}{}^{L_1}p_3(t)] + [{}^{L_1}k_{2,4}{}^{L_1}p_2(t) - {}^{L_1}k_{4,2}{}^{L_1}p_4(t)] \quad (\text{S36})$$

For an idealized case where the external concentration of the ligand is at a saturating level, whereas the internal concentration is zero, the inward transporting rate is at the theoretical maximum, commonly called k_{cat} . In a previous substrate uptake assay (Tsai et al., 2012), the concentration of nonradioactive substrate inside the vesicles was always 5 mM, whereas the initial concentration of the radioactive substrate outside the vesicles was varied. In theory, the uptake rate of radioactive substrate should increase to a maximum when the concentration of the radioactive substrate outside the vesicles was raised to a saturating level, if the net transfer of substrate molecules is so few that the changes in substrate concentrations on both sides of the vesicle membranes were negligibly small. This prediction would be reflected as an increase in the initial slope of the relation between the number of transported molecules and time (Fig. 12). This maximum rate k_{max} would, however, be less than k_{cat} obtained under the condition that one side of the membrane had a saturating concentration of substrate, whereas the other side has practically no substrate. In some cases, the average ratio of the number of AdiC to the volumes of vesicles or their bathing medium is so high that the number of AdiC molecules is not sufficiently smaller than that of substrate molecules. In that case, the concentration gradient of the ligand drops substantially during the assay, lowering the transport rate over time. If given sufficient time, the rate would approach zero, seen as the number of transported molecules approaching a plateau with time (Fig. 11, B and C), as was observed in their substrate uptake assays (Tsai et al., 2012).

Those uptake assays were performed in individual 50 μl vol, where the liposomes embedded with AdiC made up ~2% of the volume (i.e., $\text{vol}_{\text{lip}} = 1 \mu\text{l}$). Thus, the volume of solution outside the liposome (vol_{out}) was 49 μl . As an example, for the case of 50 μM radioactive Arg⁺, there should be 2.5×10^{-9} mol of it in vol_{out} . The presence of 5 mM nonradioactive Arg⁺ inside the liposomes with a total volume of about 1 μl , there should be about 5×10^{-9} mol of Arg⁺ molecules in vol_{lip} . The liposomes were incorporated with 6.5 μg of the AdiC protein, translated to 6.5×10^{-11} mol of AdiC dimers (100 kDa) or 1.3×10^{-10} mol of monomers. In a given assay, only the molecules in either the inside-out or the outside-out orientation were examined, molecules were approximately randomly oriented in the two orientations. Thus, on a subunit basis, the effective number of AdiC was reduced by half to 6.5×10^{-11} mol. The estimated molar ratio of external radioactive Arg⁺ to AdiC monomer would be calculated as $\frac{2.5 \times 10^{-9} \text{ mol}}{6.5 \times 10^{-11} \text{ mol}} = 38$, and that of the internal nonradioactive Arg⁺ as $\frac{5.0 \times 10^{-9} \text{ mol}}{6.5 \times 10^{-11} \text{ mol}} = 76$. These ranges of substrate molecules per AdiC are expected from Eqs. S37 and S38 to lead to a time-dependent change in the concentrations, which is manifested as a reduction in the transport rate, i.e., the derivative of the curve, over time. Consistent with this expectation, the number of transported molecules indeed approached a plateau with time in their assays (Tsai et al., 2012).

Regarding the net radioactive substrates transported into the vesicles, we calculated the transport rate with the 24-state model under the conditions that the ligand concentration was time dependent (Figs. 12, 13, 14, 15, S8, S9, S10, and S11):

$$L_{1,\text{ext}}(t_{i+1}) = L_{1,\text{ext}}(t_i) - \frac{1}{\text{vol}_{\text{ext}}} {}^{L_1}\text{Flux}_{2,6}[t_i, L_1(t_i), L_2(t_i)] \cdot \Delta t \quad (\text{S37})$$

$$L_{1,\text{int}}(t_{i+1}) = L_{1,\text{int}}(t_i) - \frac{1}{\text{vol}_{\text{int}}} {}^{L_1}\text{Flux}_{3,7}[t_i, L_1(t_i), L_2(t_i)] \cdot \Delta t \quad (\text{S38})$$

where t is a discretized series of time in increments of Δt , and vol_{int} and vol_{ext} indicate the interior and exterior volumes. Calculation of the time-dependent ligand uptake would require iteratively calculating $L_{1,\text{ext}}(t_i)$ and $L_{1,\text{int}}(t_i)$, with which the uptake at each time t_i , i.e., ${}^{L_1}\text{Flux}_{2,6}(t_i, L_1(t_i), L_2(t_i))$, could then be calculated (Eqs. S37 and S38). We also calculated the Arg⁺-Agm²⁺ counter transport across bacteria membranes under the conditions that the ligand concentration was time dependent (Iyer et al., 2002) (Fig. 14). The initial Arg⁺ in the bacteria culture medium was set at 1 mM to match the reported condition. The enzyme AdiA rapidly would convert it to an Agm²⁺ that was then transported out of the bacterium. Initial interior concentration of Arg⁺ was set to 0.4 mM and Agm²⁺ to 0.05 mM (Hamana, 1996; Bennett et al., 2009; Guo et al., 2013; Sajed et al., 2016). Bacterial volume was estimated as $1.2 \times 10^{-15} \text{ L}$ and

cell density as 2×10^{11} cells/liter (Iyer et al., 2002), allowing us to calculate the external versus the total internal volumes. Over time, the concentration of Arg^+ dropped, whereas that of Agm^{2+} rose with their sum staying around 1 mM in our calculation (Fig. 14), which is in a good agreement with their experimental observation (Iyer et al., 2002).